

NL

END
DATE
FILMED
-10-30
DTIC

AFWAL-TR-80-3061

LEVEL II

1
12
H

HOLOGRAPHIC INVESTIGATION OF SLENDER BODY VORTEX WAKES

AD A089496

F. D. Deffenbaugh and J. L. Jacoby
TRW Systems and Energy
One Space Park
Redondo Beach, Ca. 90278

DTIC
ELECTE
SEP 25 1980
S D A

July 1980

Final Report for Period 28 July 1977 - 28 March 1980

Approved for Public Release
Distribution Unlimited

DDC FILE COPY

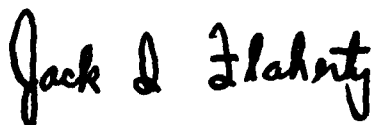
Prepared for
FLIGHT DYNAMICS LABORATORY
Wright Aeronautical Laboratories
Air Force Systems Command
Wright-Patterson AFB, Ohio 45433

80 9 25 003

NOTICE

When Government drawings, specifications, or other data are used for any purpose other than in connection with a definitely related Government procurement operation, the United States Government thereby incurs no responsibility nor any obligation whatsoever; and the fact that the Government may have formulated, furnished, or in any way supplied the said drawings, specifications, or other data, is not to be regarded by implication or otherwise as in any manner licensing the holder or any other person or corporation, or conveying any rights or permission to manufacture, use, or sell any patented invention that may in any way be related thereto.

This technical report has been reviewed and is approved for publication.

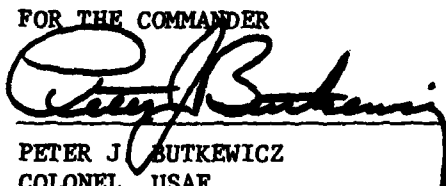


JACK I. FLAHERTY
Project Engineer
High Speed Aerodynamics Group



MELVIN L. BUCK
Chief, High Speed Aero Perf. Br.
Aeromechanics Division

FOR THE COMMANDER



PETER J. BUTKEWICZ
COLONEL, USAF
Chief, Aeromechanics Division

SECURITY CLASSIFICATION OF THIS PAGE (When Data Entered)

19 REPORT DOCUMENTATION PAGE		READ INSTRUCTIONS BEFORE COMPLETING FORM	
1. REPORT NUMBER AFWAL-TR-88-361	2. GOVT ACCESSION NO. AD-A089496	3. RECIPIENT'S CATALOG NUMBER	
4. TITLE (and Subtitle) Holographic Investigation of Slender Body Vortex Wakes	5. TYPE OF REPORT & PERIOD COVERED Final Report 28 July 78 - 28 March 80	6. PERFORMING ORG. REPORT NUMBER TRW-32399-6002-UT-00	
7. AUTHOR F. D. Deffenbaugh & J. L. Jacoby	8. CONTRACT OR GRANT NUMBER(s) F33615-78-C-3028		
9. PERFORMING ORGANIZATION NAME AND ADDRESS TRW Systems and Energy One Space Park Redondo Beach, CA 90278	10. PROGRAM ELEMENT, PROJECT, TASK AREA & WORK UNIT NUMBERS 2307N421	11. REPORT DATE July 1980	12. NUMBER OF PAGES 78
13. CONTROLLING OFFICE NAME AND ADDRESS Flight Dynamics Laboratory Wright Aeronautical Laboratories Air Force Systems Command Wright-Patterson AFB, Ohio 45433	14. MONITORING AGENCY NAME & ADDRESS (if different from Controlling Office)	15. SECURITY CLASS. (of this report) Unclassified	16. DECLASSIFICATION/DOWNGRADING SCHEDULE
16. DISTRIBUTION STATEMENT (of this Report) Approved for Public Release Distribution Unlimited			
17. DISTRIBUTION STATEMENT (of the abstract entered in Block 20, if different from Report)			
18. SUPPLEMENTARY NOTES			
19. KEY WORDS (Continue on reverse side if necessary and identify by block number) High Angle of Attack Aerodynamics Holography Flow Visualization			
20. ABSTRACT (Continue on reverse side if necessary and identify by block number) The three dimensional vortex flow field behind slender missile configurations at high angle of attack was investigated using laser holography. Holographic interferograms of the flow about two ogive cylinder models were recorded for low speed flows, $M < .1$, at angles of attack from 20 to 50 degrees. Helium injected into the flow above the model was entrained into the entire vortex structure, and the three dimensional position of the core could not be determined from the interferograms. Dual exposure holograms of the flow field seeded with 40-100 micron glass microballoons were recorded using a pulsed ruby			

DD FORM 1 JAN 73 1473 EDITION OF 1 NOV 65 IS OBSOLETE

SECURITY CLASSIFICATION OF THIS PAGE (When Data Entered)

409831

Dut

20. Abstract (Cont.)

laser. Pairs of particles could not be easily identified in the reconstructed image and the three dimensional velocity field could not be measured. Surface pressures were measured and integrated to provide load distributions, normal and side force coefficients. Roll angle was varied with angle of attack and tunnel conditions constant. Conditions of maximum vortex asymmetry were determined from the measured pressure distributions.

PREFACE

The work reported herein was conducted by the Engineering Sciences Laboratory of TRW Systems and Energy, One Space Park, Redondo Beach, California. The work was supported by the Air Force Flight Dynamics Laboratory (AFWAL/FIMG), Air Force Wright Aeronautical Laboratories, Wright-Patterson Air Force Base, Ohio 45433 under Program Element 61102F, Project/2307, Task/2307N4, and Work Unit/2307N421. We are indebted to Mr. Jack Flaherty of the Flight Dynamics Laboratory for his support throughout this effort.

5 12 -

Accession For	
NTIS GRA&I	<input checked="checked" type="checkbox"/>
DDC TAB	<input type="checkbox"/>
Unannounced	<input type="checkbox"/>
Justification	
By	
Distribution/	
Availability Codes	
Dist	Avail and/or special
A	

TABLE OF CONTENTS

	<u>Page</u>
1.0 INTRODUCTION	1
2.0 HOLOGRAPHIC FLOW VISUALIZATION	3
2.1 Double Exposure Holographic Interferometry.	5
2.2 Rapid Double Pulse Holography	7
3.0 TEST APPARATUS	9
3.1 Test Facility	9
3.2 Test Article and Support System	9
3.3 Instrumentation	9
4.0 TEST PROCEDURE	25
4.1 Test Conditions and Technique	25
4.2 Data Reduction.	26
5.0 RESULTS.	36
6.0 DISCUSSION	57
7.0 CONCLUSIONS AND RECOMMENDATIONS.	62
REFERENCES.	64

LIST OF ILLUSTRATIONS

<u>Figure</u>	<u>Page</u>
1. Basic Arrangements for Recording and Reconstructing Transmission Holograms	4
2. Wind Tunnel Model Installation	10
3. Wind Tunnel Model Support and Coordinate System.	12
4. Y_T , Z_T Support System.	13
5. Static Pressure Tap Locations Looking Upstream	14
6. Body Pressure Tap Locations.	15
7. Angular Position θ , of Pressure Taps Measured Relative to the Wind Vector as a Function of Roll Angle, ϕ	16
8. Dual Reference Beam Transmission Holography.	18
9. Model Coordinate System.	20
10. Dual Reference Beam Reconstruction System for Particle Tracking	21
11. Camera Arrangement for Recording the Virtual Image of Reconstructed Hologram.	24
12. Wind Tunnel Models	33
13. Delta Wing at 45 Degrees Angle of Attack, Front View Along Body x-Axis.	33
14. Delta Wing at 45 Degrees Angle of Attack, Side View.	34
15. Delta Wing at 45 Degrees Angle of Attack, Front View Along Free Stream Direction.	34
16. Effect of Roll Angle on N4B2 Side Force Coefficient.	37
17. Effect of Roll Angle on N4B2 Normal Force Coefficient.	38
18. Pressure Distribution on N4B2, Run 3, Angle of Attack $\alpha=45^\circ$	39
19. N4B2 Interferogram Focused at Station 2, $x/d = 4.80$, Angle of Attack, $\alpha=45^\circ$	42
20. Pressure Distribution on N4B2, Run 7, Angle of Attack $\alpha=45^\circ$	42

LIST OF ILLUSTRATIONS (Continued)

<u>Figure</u>	<u>Page</u>
21a. N4B2 Interferogram Focused at Station 1, $x/d = 1.92$, Angle of Attack, $\alpha=50^\circ$	44
21b. N4B2 Interferogram Focused at Station 2, $x/d = 4.80$, Angle of Attack, $\alpha=50^\circ$	44
22. Pressure Distribution on N4B2, Run 9, Angle of Attack $\alpha=50^\circ$	45
23. N4B2 Side Force Coefficient Variation With Angle of Attack	46
24. N4B2 Normal Force Coefficient Variation With Angle of Attack	47
25. N2B1 Side Force Coefficient Variation With Angle of Attack	48
26. N2B1 Normal Force Coefficient Variation With Angle of Attack	49
27. Normal Force Distribution on N2B1 at 45 Degrees Angle of Attack.	50
28. Pressure Distribution on N2B1, MX Run 327, Angle of Attack, $\alpha=45^\circ$	51
29. Pressure Distribution on N2B1, Run 13, Angle of Attack $\alpha=45^\circ$	53
30. N2B1 Interferogram Focused at Station 1, $x/d = 2.83$, Angle of Attack, $\alpha=45^\circ$	53
31. Pressure Distribution on N2B1, Run 18, Angle of Attack $\alpha=30^\circ$	54
32. Pressure Distribution on N2B1, Run 21, Angle of Attack $\alpha=20^\circ$	55
33. N2B1 Interferogram Taken From the Side, Angle of Attack $\alpha=30^\circ$	56

1

LIST OF TABLES

<u>Table</u>	<u>Page</u>
1. Model Geometry and Instrumentation	11
2. Test Matrix.	27

NOMENCLATURE

a	Maximum body radius = $d/2$
C_d	Sectional normal force coefficient, $\frac{\text{Normal Force Per Unit Length}}{q_\infty d}$
C_ℓ	Sectional side force coefficient, $\frac{\text{Side Force Per Unit Length}}{q_\infty d}$
CN	Normal force coefficient, $N/q_\infty S$
CY	Side force coefficient, $Y/q_\infty S$
C_{m_o}	Pitching moment about the nose, $M/q_\infty S\ell$
C_m	Pitching moment about $(0, 0, \lambda)$
C_{n_o}	Yawing moment about the nose, $MY/q_\infty S\ell$
C_n	Yawing moment about $(0, 0, \lambda)$
C_p	Three dimensional coefficient of pressure, $P-P_\infty/q_\infty$
d	Maximum body diameter
f	Fineness ratio, ℓ/d
ℓ	Body length
ℓ_n	Nose length
ℓ_{cyl}	Cylindrical Afterbody length
M	Pitching moment
N	Normal force
P	Surface Pressure
q_∞	Free stream dynamic pressure, $1/2\rho V^2$
q	Cross flow dynamic pressure, $1/2\rho U^2$

Re_d	Reynolds number based on diameter
Re_∞	Free stream unit Reynolds number
R	Three dimensional body radius
R_o	Tangent ogive radius
r_n	Nose radius
S	Frontal area, $\pi d^2/4$
U	Cross flow velocity, $V \sin \alpha$
V	Free stream velocity
W	Axial component of free stream velocity, $V \cos \alpha$

Aeroballistic Coordinate System (origin missile nose)

X	Positive pointing aft from missile nose, $X = X_B$
Y	Perpendicular to angle of attack plane
Z	Positive pointing up in the angle of attack plane

Fixed Body Coordinate System (origin missile nose)

X_B	Pointing aft along body axis
Y_B	Lateral body coordinate aligned with 0 degree engraving mark on missile model
Z_B	Perpendicular to X_B , Y_B

Body Center of Rotation Coordinate System (origin at center of rotation of missile, see Figure 3)

X_R	Positive pointing aft
Y_R	Lateral coordinate, parallel to Y_B , aligned with 0 degree engraving mark on missile
Z_R	Perpendicular to X_R , Y_R

Tunnel Axis System (origin at model center of rotation), see Figure 3

X_T Positive in wind direction
 Y_T Positive to the right looking upstream
 Z_T Perpendicular to X_T , Y_T

Wall Axis System (origin centered on tunnel wall)

X_W Positive pointing downstream
 Y_W Positive to the right looking upstream
 Z_W Perpendicular to X_W , Y_W

Laser Axis System (origin = wall axis origin)

X_L Perpendicular to X_L , Y_L
 Y_L Positive along laser axis
 Z_L $Z_L = Z_W$

Flow Velocities

u Flow velocity in X direction
 v Flow velocity in Y direction
 w Flow velocity in Z direction

Optics

A Time dependent wave amplitude
 A_R Time dependent reference beam wave amplitude
 A_S Time dependent scene beam wave amplitude
 A_{OUT} Wave amplitude of reconstructed hologram

I	Intensity
I_v	Intensity of virtual image
L	Optical pathlength
T	Transmission of the hologram
a	Time independent wave amplitude
a_R	Time independent reference beam wave amplitude
a_S	Time independent scene beam wave amplitude
t	Time
t_E	Exposure time
n	Index of refraction
κ	Constant relating to properties of film emulsion
ω	Frequency of light
ϕ	Phase of light wave
λ	Optical wavelength

Greek

α_T	Total angle of attack; angle between the X_B axis and wind vector
ϕ	Body roll angle, angle from windward ray to Y_B axis, measured positive as a right hand rotation of Y_B to Z_B
θ	Angle of pressure tap relative to wind vector
θ_o	Angle of pressure tap relative to fixed body coordinates (Y_B Z_B)
μ	Support system pitch angle
ν	Support system yaw angle

- τ Support system roll angle
- ζ Angle between missile roll axis and support system yaw axis
Fixed at $\zeta = 28^\circ$
- Γ Circulation $\Gamma = \oint \bar{u} \cdot ds$

Sub and Superscript

- ()^{*} Denotes dimensional quantities
- ()^o Particle position or velocity

1.0 INTRODUCTION

Previous experimental investigations of the flow behind a missile at high angle of attack have shown that the asymmetric vortex wake and resulting side force is sensitive to roll angle and tunnel turbulence level (1-4). In addition, it is known that for some angles of attack, the vortices may be bi-stable; the asymmetric vortex structure may suddenly switch from one stable state to another (3-5). The sensitivity of the vortex structure has so far prevented the development of adequate prediction techniques for angles of attack between about 35 and 70 degrees.

Three dimensional holographic visualization of incompressible fluid flow about an aerodynamic shape offers a potentially important diagnostic technique for wind tunnel studies. For the high angle of attack problem, holography is an optical technique which records a volume of information and may permit in situ measurement of the flow.

Laser Doppler techniques have been used by several researchers to investigate the high angle of attack body vortex flow field (6-8). Unfortunately laser Doppler techniques are single point measurements and are not useful for measuring three dimensional unsteady flows. The use of rapid double pulse holography provides a means by which an instantaneous picture of the three dimensional flow can be obtained in an unsteady condition (9).

In the present study, hollow glass microballoons were injected into the flow and rapid double pulse holography was used to record the particle positions in three dimensional space. However, difficulties encountered in switching reference beams resulted in usable data for only one of the exposures and precluded tracking the particles using the present optical reconstruction system.

Two ogive cylinder wind tunnel pressure models were tested in TRW's low speed wind tunnel at Mach number, $M < .1$, and angles of attack from 20 to 50 degrees. Measured surface pressure data was integrated to provide normal and side force coefficient data. Roll angle was varied to produce maximum and minimum vortex asymmetries and values of side force coefficient.

Interferometric holograms were taken to visualize the vortex flow structure. Interferograms taken looking directly down the missile axis showed core locations which could be correlated with the measured pressure distributions.

2.0 HOLOGRAPHIC FLOW VISUALIZATION

Optical holography is a process which records both the amplitude and the phase distributions of an optical wavefront which has interacted with a scene. The recording, called a hologram, is made on a high resolution, photographic emulsion. The image retrieval process, termed reconstruction, reproduces the wavefronts of the light as they existed during the original exposure. In viewing the reconstructed hologram, the observer sees a true three-dimensional representation of the original scene.

Figure 1 shows the basic arrangement for recording and reconstructing transmission holograms. The hologram is recorded through the interaction of two light beams, the object (or scene) beam and the reference beam which are mutually coherent*. The reference beam is usually a simple spherically expanding beam so that it can be easily reproduced during the reconstruction process. The laser serves as the common source for both beams which are separated by means of a beam splitter.

For purposes of holographic flow visualization, the object wave is a light beam which transmits the fluid flow scene. The reference beam bypasses the flow and is incident in the holographic plane at a certain angle. Both light waves are recorded on a holographic plate by a photographic emulsion process which is sensitive only to the intensity or energy of the light. The light beam which is emitted by the laser can be represented as a wave amplitude (10-12),

$$A = ae^{i\omega t} \quad (1)$$

which is split into the scene and reference beam as

$$A_R = a_R e^{i\omega t} \quad (2)$$

and

$$A_S = a_S e^{i\omega t} \quad (3)$$

* Coherence means that a definite, stable phase relationship exists between different parts of the beam.

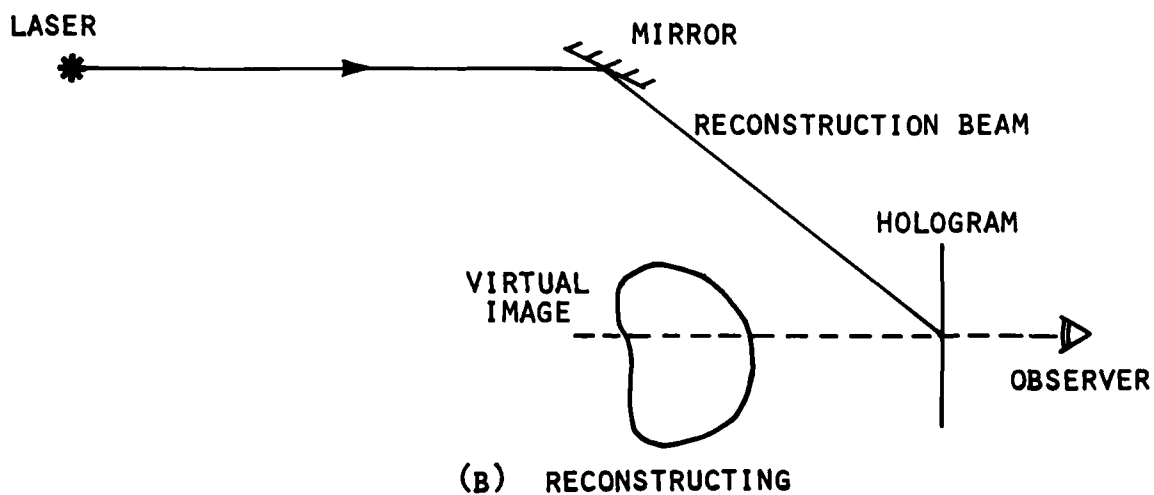
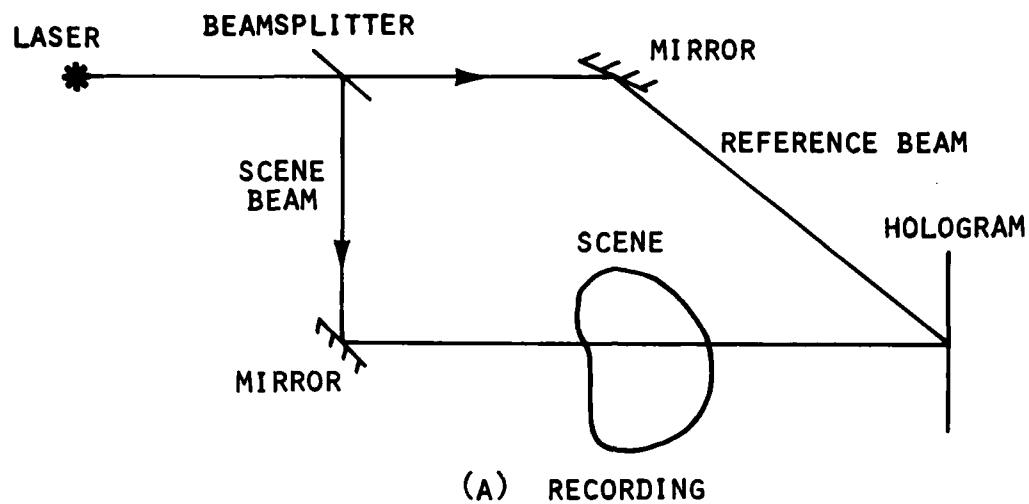


Figure 1. Basic Arrangements for Recording and Reconstructing Transmission Holograms

Then the intensity recorded on the plate is

$$I = |A|^2 = |A_R + A_S|^2 = (A_R + A_S)(A_R^* + A_S^*) \quad (4)$$

where the asterisks denote the complex conjugate. A linear photographic media after exposure to the scene and reference beams will have the following transmission pattern $T = 1 - \kappa t_E$ where κ is a property of the emulsion and t_E is the exposure time. Illumination of the holographic plate with a duplicate of the reference beam then recreates the light pattern

$$\begin{aligned} A_{OUT} &= A_R T \\ &= [1 - \kappa t_E (a_R a_S^* + a_S a_R^*)] A_R - \kappa t_E a_R a_S^* A_R - \kappa t_E a_R^* a_S A_R \end{aligned} \quad (5)$$

The last term is proportional to the original wavefront since

$$\kappa t_E a_R^* a_S A_R = \kappa t_E a_R^* a_S a_R e^{i\omega t} = \kappa t_E a_R^* a_R a_S e^{i\omega t} = \kappa t_E a_R^* a_R A_S \quad (6)$$

The scene beam has been altered only the multiplicative constant

$$-\kappa t_E a_R^* A_R \quad (7)$$

The other two components of the reconstructed wavefront represent the unchanged reconstruction wave and the conjugate scene beam.

The last term of the reconstruction presents the viewer with a virtual image which is indistinguishable from the original scene. The intensity of the virtual scene is

$$\begin{aligned} I_V &= |-\kappa t_E a_R^* a_R A_S|^2 \\ &= \kappa^2 t_E^2 |a_R|^4 |A_S|^2 \end{aligned} \quad (8)$$

2.1 Double Exposure Holographic Interferometry

If the holographic plate is exposed twice to the same reference beam pattern but slightly different scene wave fronts, the transmission recorded

on the plate will be

$$T = 1 - \kappa t_E (I_1 + I_2) \quad (9)$$

where I_1 is the intensity pattern due to the first exposure and I_2 is the intensity pattern due to the second exposure. Reillumination of this pattern with the reference beam yields a virtual image where intensity is now

$$\begin{aligned} I_V &= |\kappa t_E a_R a_R^* (A_{S1} + A_{S2})|^2 \\ &= \kappa^2 t_E^2 |a_R|^4 (A_{S1} + A_{S2})(A_{S1}^* + A_{S2}^*) \end{aligned} \quad (10)$$

If the flow in the scene changes the phase of the light waves from one exposure to the next such that

$$A_{S1} = a_S e^{i\phi_1} \quad (11)$$

$$A_{S2} = a_S e^{i(\phi_1 + \Delta\phi)} \quad (12)$$

then the intensity of the virtual image is

$$I_V = \kappa^2 t_E^2 |a_R|^4 |a_S|^2 (2 + e^{i\Delta\phi} + e^{-i\Delta\phi}) \quad (13)$$

or

$$I_V = 2\kappa^2 t_E^2 |a_R|^4 |a_S|^2 (1 + \cos(\Delta\phi)) \quad (14)$$

and the scene intensity varies as the cosine of the change in phase of the scene beam. Phase shifts of 180° will appear as black fringes within the scene.

The changes in phase of the optical wavefronts recorded by holographic interferometry are the result of changes in the optical path length traversed by the scene beam. The optical path length, $L = \int_{\text{physical path}} n(x) dx$, is a function of both the physical path traversed and the index of refraction along this path. The phase changes at the hologram are related to the path length changes by $\Delta\phi = \frac{2\pi\Delta L}{\lambda}$. Since the physical path length is a constant in this experiment, variations in refractive index were required to produce interference patterns which would describe the flow field. To

visualize the vortex flow field, helium gas ($n_{\text{He}}=1.000036$, $n_{\text{air}}=1.000293$) was injected into the flow after the first exposure of the holographic plate. The helium was entrained into the vortex structure and thus shifted the phase of light passing through the structures during the second exposure, i.e., $\Delta\phi = \frac{2\pi}{\lambda} \int (n_{\text{He}} - n_{\text{air}}) dx$ where n_{He} is dependent on the helium concentration. Upon reconstruction, the three-dimensional interference fringe patterns observed indicated the distribution of the helium within the vortex structure.

2.2 Rapid Double Pulse Holography

Fluid velocity measurements in three dimensions by particle tracking is possible using holography. If the flow is seeded with small particles and a double exposure of the fluid scene is made with a well defined time interval, then the velocity field can be determined from the reconstructed image provided that particle identification in both exposures can be determined. The reconstructed flow field contains the spatial distribution of particles at two instants in time. The accuracy of the velocity measurements will depend on the particle size, particle concentration, and the accuracy with which the timing of the laser pulses is known. Note that this technique differs from holographic interferometry as no changes in the optical path length have been introduced.

For particles to follow streamlines in a vortex flow, small particle sizes $\phi \leq 5$ microns are required. However particles that are too small scatter less light and are difficult to record. The resolution after reconstruction depends upon the resolution by the photographic emulsion and importantly on the distance between the particle and recording plane. At present, particle sizes of about 100 microns seem to be an optimum.

The time between pulses is determined by the flow quantities to be measured. The pulse time must be chosen such that a particle has been able to move a few diameters from its original position yet not so far away that particle identification becomes difficult.

In order to holographically record high speed events, it is necessary to use a pulsed laser such as a ruby laser. When operated in the Q-switched mode, the ruby laser produces short pulses having large peak powers. The pulse durations, typically on the order of 30 to 50 nanoseconds, are short

enough to effectively "stop" the motion of many high speed events. Peak powers on the order of 10^8 watts may be produced during these short pulses, thus providing sufficient light for illuminating fairly large scenes. Ruby lasers can be made to exhibit good coherence properties, another requirement for recording large scenes. The ruby laser produces light in the visible spectrum ($\lambda = 694.3$ nm, deep red) which means that standard optical components can be used to process the light and that some standard photographic emulsions can be used in the recording process. Furthermore, little distortion is introduced when the holograms are viewed with continuous wave lasers such as HeNe lasers. The HeNe laser operates at a wavelength of 632.8 nm which is fairly close to the ruby wavelength.

3.0 TEST APPARATUS

3.1 Test Facility

TRW's low speed wind tunnel is a vertically-oriented recirculating facility capable of operating at velocities of up to 80 ft/sec in the 11 x 11 inch test section.

An installation photograph of the N2B1 model is shown in Figure 2.

3.2 Test Article and Support System

Two ogive cylinder models were used in the present tests. The models are geometrically similar to the N4B2 and N2B1 models used in the MX (13) tests but are based on a 1 inch diameter. Model dimensions are presented in Table 1.

Two support systems were used in the present study. The support system shown in the sketch in Figure 3 and in the installation photograph Figure 2 allowed for model pitch, yaw, and roll about a center of rotation near the centerline of the wind tunnel. The system was designed so that the model could be positioned at the desired angle of attack with a yaw angle chosen to prevent the model from blocking the laser scene beam.

A second support system was used which allowed the model to be pitched only in the Y_T , Z_T plane, Figure 4. With the second support system the fixed laser axis system was coincident with the model axis system and afforded a cross-flow view of the vortex structure.

3.3 Instrumentation

Pressures

The wind tunnel models were instrumented each with 48 pressure taps as shown in Figures 5 and 6. The angular position of the tape with respect to the cross flow wind direction as a function of the roll orientation is indicated in Figure 7. The pressure data were obtained using an externally mounted 48 port Scanivalve connected to a single ± 0.1 psi differential pressure transducer. Stainless steel pressure tubes extending from the surface taps to the model base were connected to the Scanivalve using 1/32 inch plastic tubing. The plastic tubing was routed through a hole in the wind tunnel wall. The total length of the tubing was less than 3 feet. Pressures read on a digital voltmeter were entered into a data



Figure 2. Wind Tunnel Model Installation

TABLE 1. MODEL GEOMETRY AND INSTRUMENTATION

Configuration	Tangent Ogive Radius	Nose Length	Nose Radius	Cylinder Length	Overall Length	d (inches)	Pressure Stations (x/d)		
	$\frac{R_o}{d}$	$\frac{\ell_n}{d}$	$\frac{r_n}{d}$	$\frac{\ell_{cyl}}{d}$	$\frac{\ell_n + \ell_{cyl}}{d}$		1	2	3
N2B1	7.0	2.545	.03	7.754	10.3	1.0	2.83	4.80	8.75
N4B2	3.0	1.633	.03	6.461	8.094	1.0	1.92	4.80	6.54

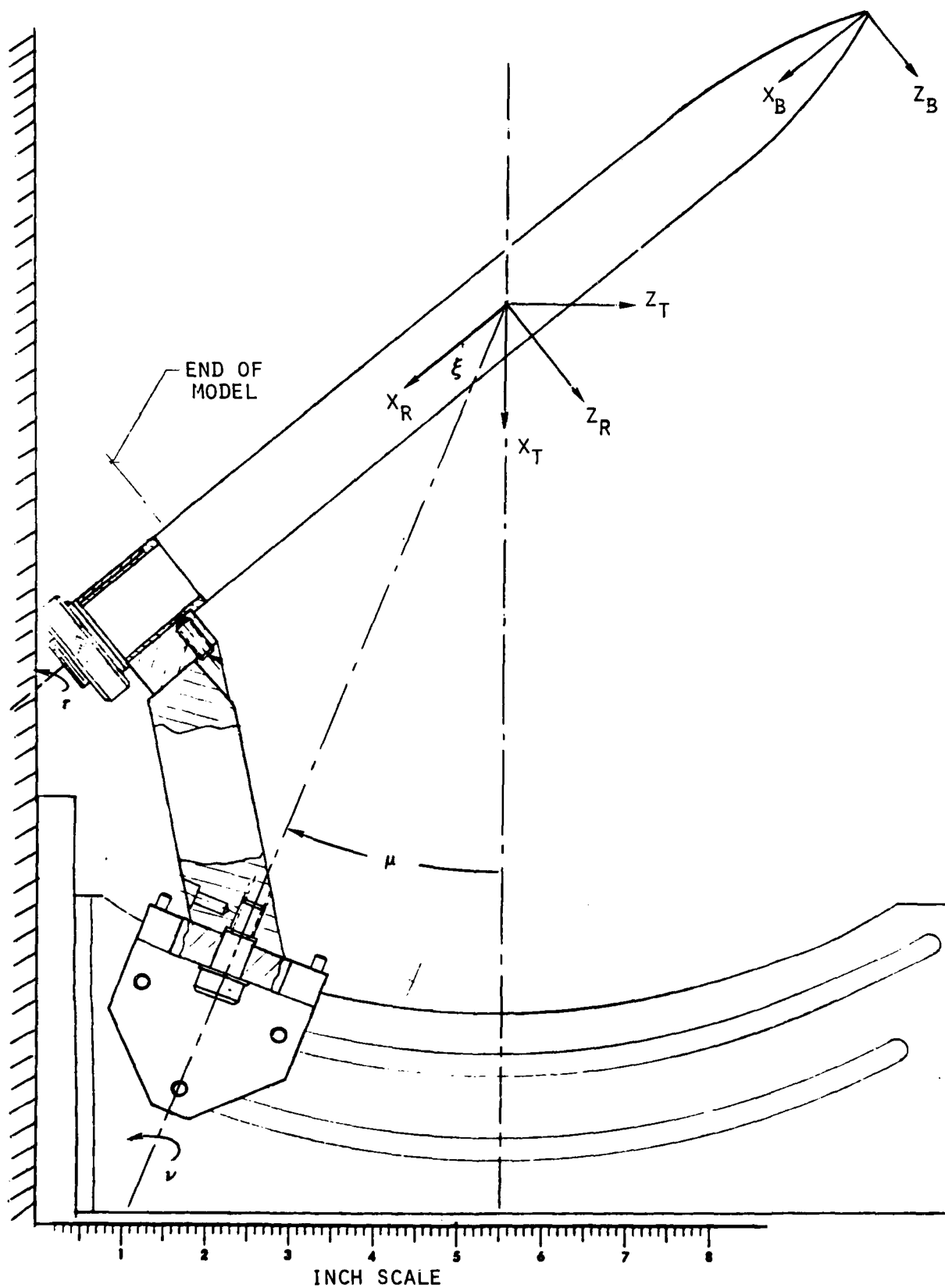


Figure 3. Wind Tunnel Model Support and Coordinate System

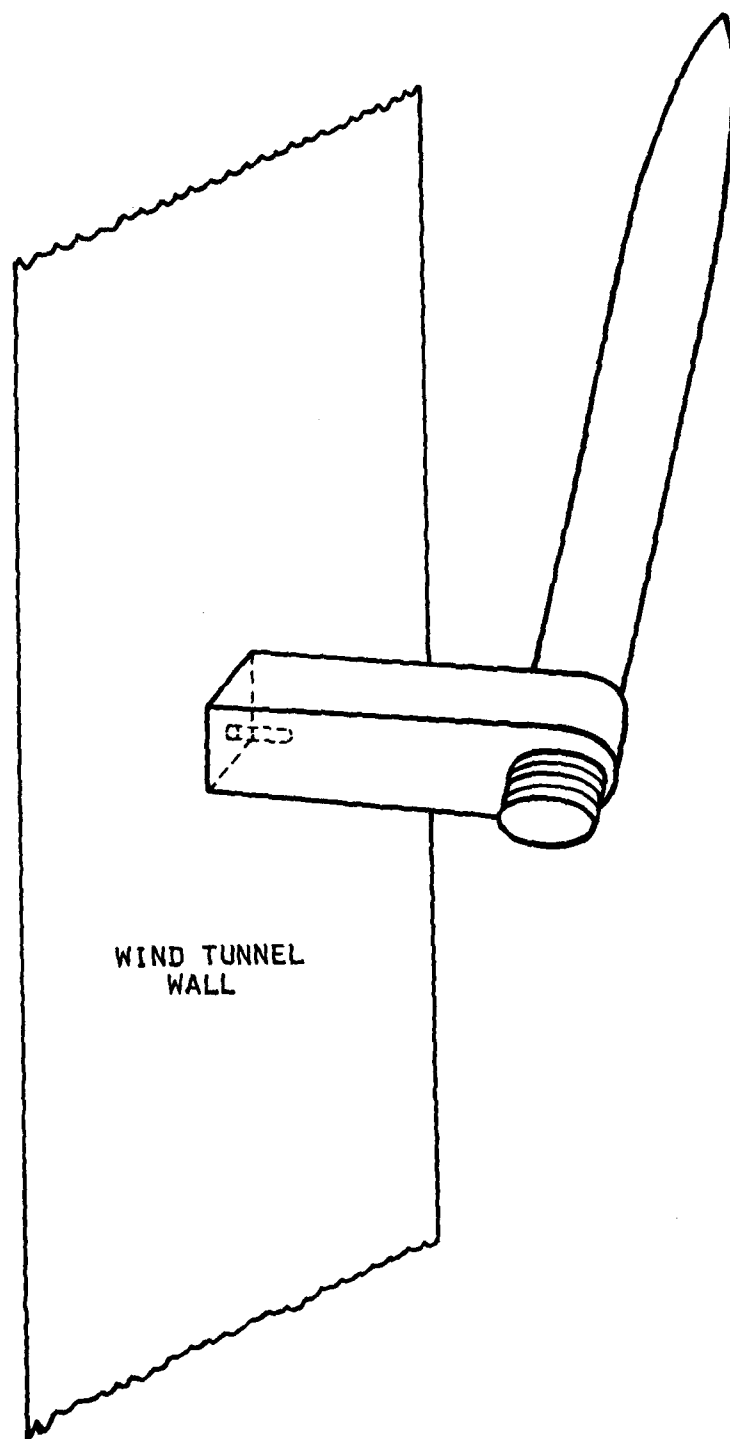
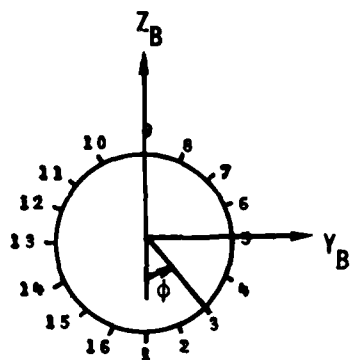


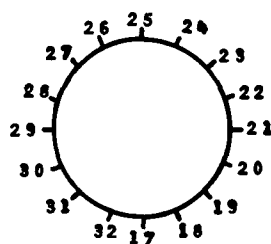
Figure 4. Y_T , Z_T Support System



N2B1 $x_B/d = 2.83$

N4B2 $x_B/d = 1.92$

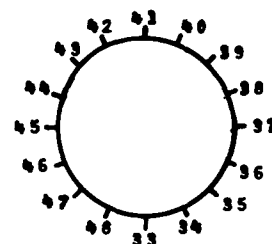
STATION 1



$x_B/d = 4.80$

$x_B/d = 4.80$

STATION 2



$x_B/d = 8.75$

$x_B/d = 6.54$

STATION 3

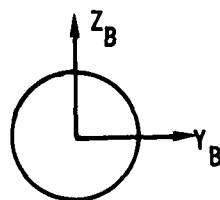
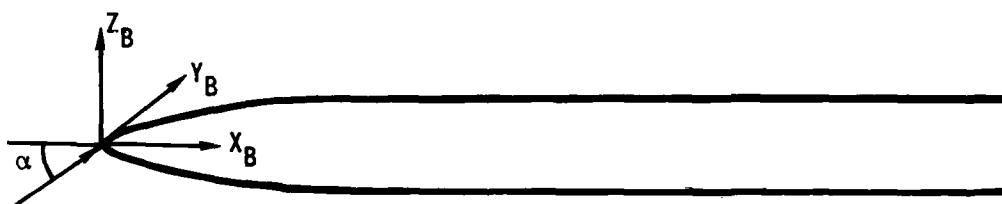
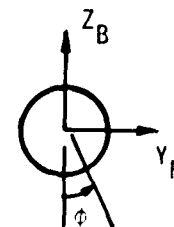
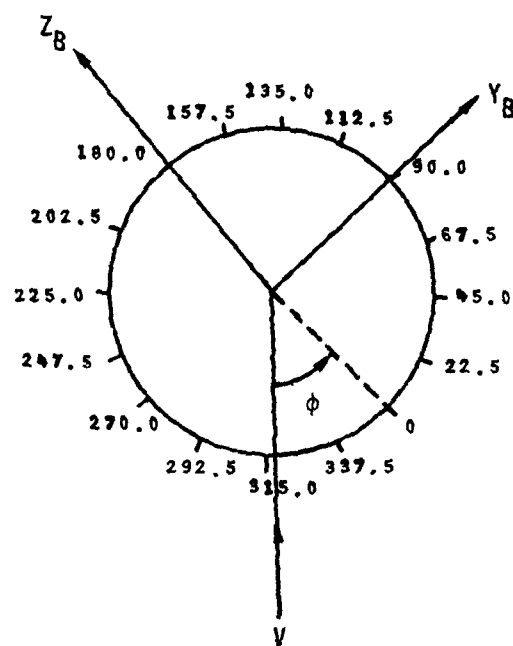


Figure 5. Static Pressure Tap Locations Looking Upstream



$\theta_0 \backslash x_B/d$	BODY PRESSURE TAPS		
N2B1	2.83	4.80	8.75
N4B2	1.92	4.80	6.54
0	1	17	33
22.5	2	18	34
45.0	3	19	35
67.5	4	20	36
90.0	5	21	37
112.5	6	22	38
135.0	7	23	39
157.5	8	24	40
180.0	9	25	41
202.5	10	26	42
225.0	11	27	43
247.5	12	28	44
270.0	13	29	45
292.5	14	30	46
315.0	15	31	47
337.5	16	32	48

Figure 6. Body Pressure Tap Location



$$\theta = \theta_0 + \phi$$

Figure 7. Angular Position, θ , of Pressure Taps Measured Relative to the Wind Vector as a Function of Roll Angle, ϕ .

acquisition program via a remote terminal interfaced with the CDC 6600 computer. Each pressure reading was entered into the program at the terminal and then the Scanvalue was advanced a step to take the next reading until all 48 values had been entered. The data acquisition program computed and printed on line, tunnel test conditions, pressure coefficients, load distribution, normal and side forces.

Dual Reference Beam Transmission Holography Optics

The specific optical components used, as well as their relative orientations, will vary with the scene under study as well as the form of data desired. Figure 8 shows the optical arrangement for recording the flow in the wind tunnel which was used for this program. The various prisms and lenses serve to direct the beams to the holographic plate. The route of the three beams is determined by the condition that the pathlength for each, from the laser to the hologram, must be equal.

The light emitted by the ruby laser is directed through a polarizer and a Pockels cell. The polarizer assures that the light is linearly polarized. The Pockels cell, when energized, will rotate the plane of polarization by 90°. This will enable the reference beam to be switched between two separate paths. The beamsplitter reflects approximately 4% of the light into the reference beams. The transmitted beam becomes the scene beam. It is expanded and collimated before being directed through the test section of the wind tunnel to the hologram. The reference beam, which was reflected from the beamsplitter, is directed to a polarizing beamsplitter. This element directs the reference beam along one path or the other depending on the plane of polarization of the beam. This is determined by the Pockels cell. The two reference beams are expanded and collimated. They are then routed around either side of the test section and finally directed to the hologram by mirrors.

The hologram produced by the interaction of the scene beam with one reference beam produces a record of the particular distribution in the flow at a particular instant in time. A second hologram on the same film plate is recorded shortly thereafter (~ 200 μ secs) using the same scene beam but the other reference beam. This is accomplished by pulsing the laser twice and switching the state of the Pockels cell between the two pulses.

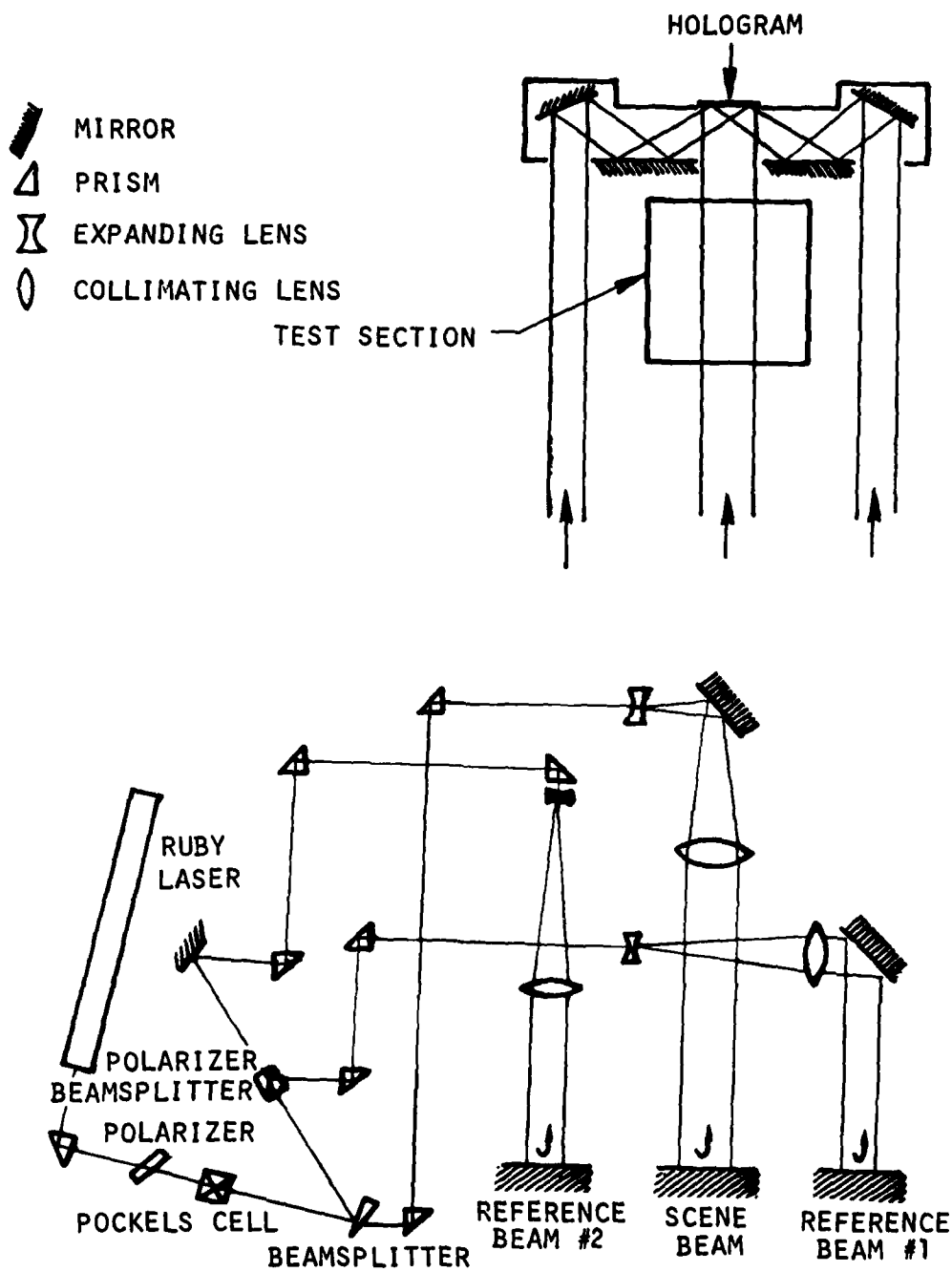


Figure 8. Dual Reference Beam Transmission Holography

The holographic image can only be reconstructed with a beam which impinges on the hologram with the same angle as the recording reference beam. The two images are thus completely independent and can be viewed either singly or superimposed by selecting the direction of the reconstruction beam. Flow velocities may be subsequently determined by measuring particle displacements between the two holographic exposures.

The acceptable orientation of the model in the wind tunnel is constrained by the requirement that the volume of interest be; 1) illuminated by the laser and 2) viewable from the position of the hologram. The small microballoons needed to track the flow can only be viewed by a form of forward light scattering, i.e., reflection of light from the particles is not practical. It is therefore unavoidable that some part of the scene will be blocked from view by the opaque model and that another part of the scene will be in the shadow of the model. The optics must be configured so that the areas of interest are properly illuminated and not obscured. The optical system was designed so that the scene beam was aligned at a 45 degree angle with respect to the vertical axis of the tunnel.

In the installation photo, Figure 2, the beam is directed from the lower window port to the upper port. The holographic plate (not shown) was positioned just on top of the I-beam tunnel support structure (seen at the top of the photo). The view from the hologram was thus looking down at a 45° angle. With the model set for a 45° angle of attack, it was possible to look directly down the model axis, see Figure 9.

The optical arrangement for reducing the particle data is illustrated in Figure 10. A 15 mw HeNe laser was employed because it has a continuous beam, produces enough light to yield a bright image which can be easily viewed and photographed, and its wavelength (632.8 nm) is sufficiently close to the wavelength of the ruby laser with which the holograms were made so as to introduce little distortion into the reconstruction process. The spatial filter/collimator produces a clean, uniform beam having a 50 mm diameter. Since it was desired to be able to look at either image separately or superimpose one over the other, a 50% beam splitter was used to produce two identical beams which could be independently shuttered. The two sets of lenses served both to focus the beams through the small apertures of the shutters and to increase the diameters of the beams to about 80 mm. The

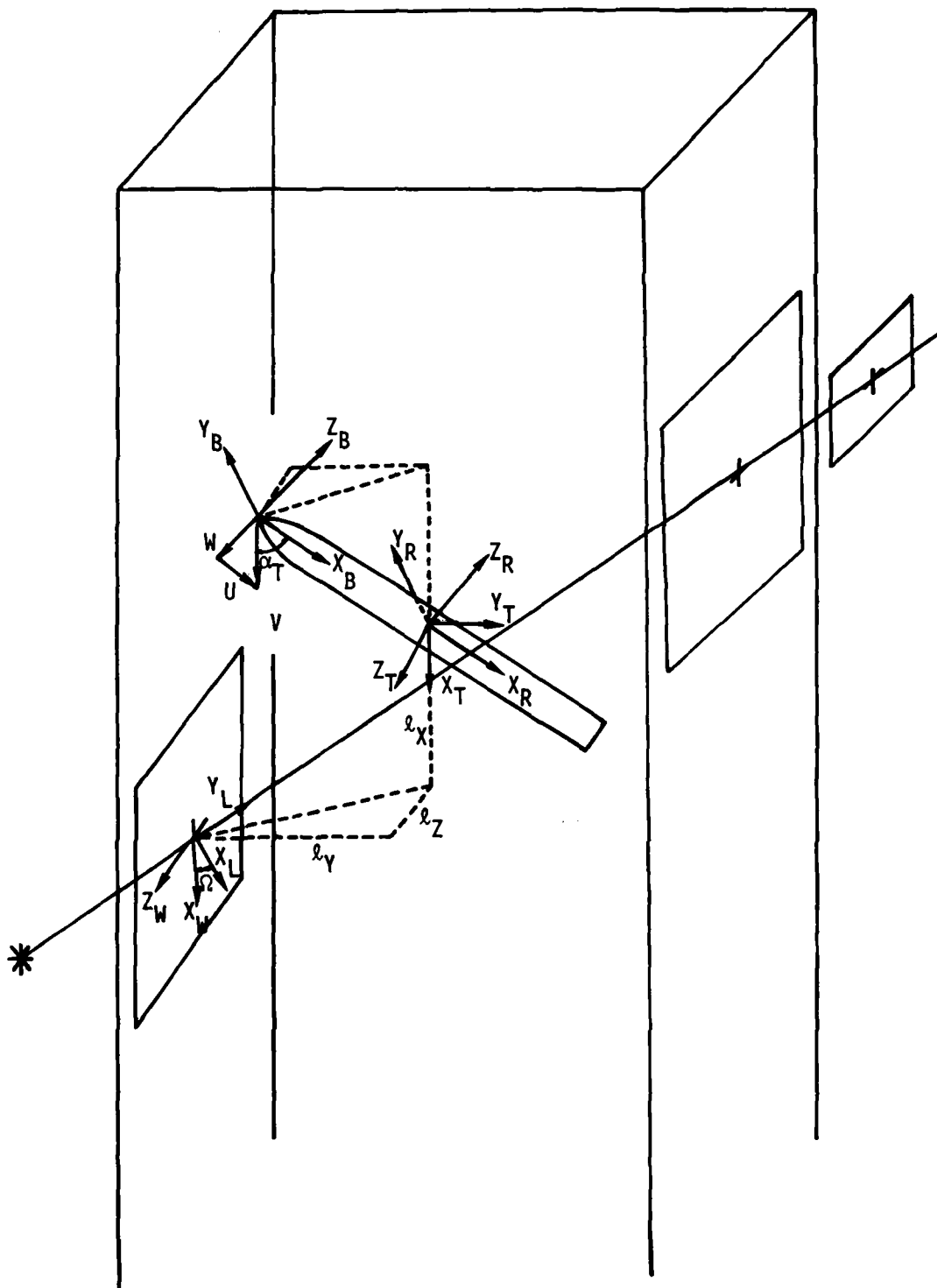


Figure 9. Model Coordinate System

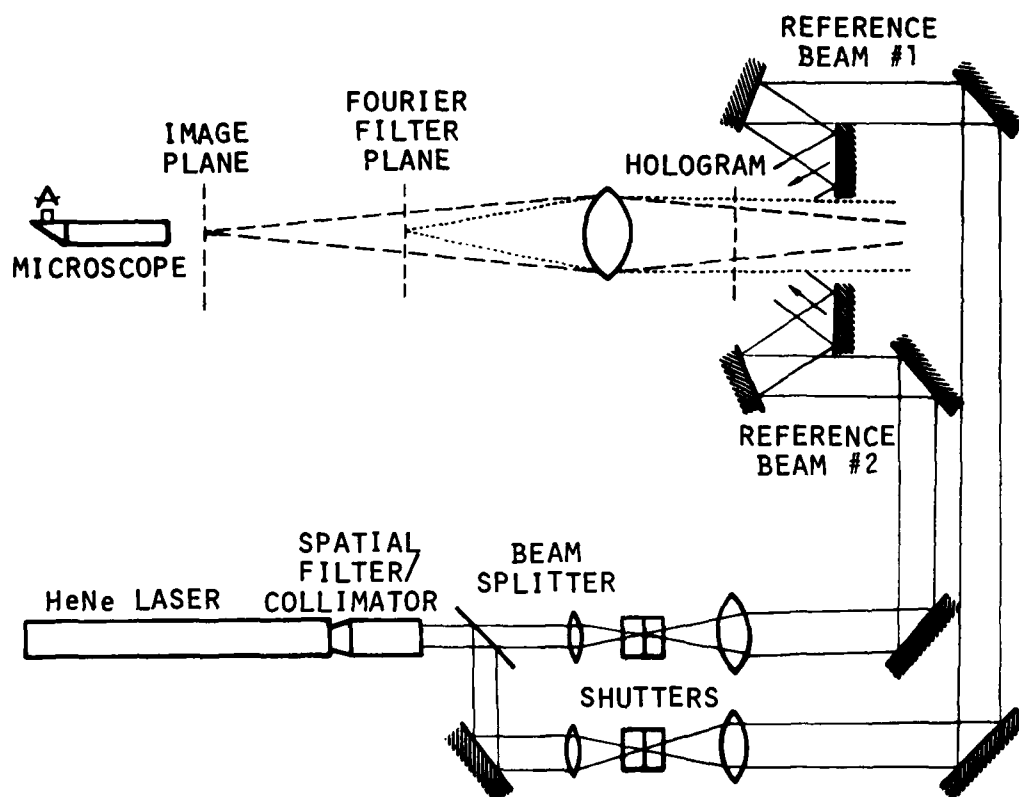


Figure 10. Dual Reference Beam Reconstruction System for Particle Tracking.

two beams were then routed to the hologram along separate paths which closely paralleled those used when the hologram was made. The mirrors in the beam paths have fine adjustment which allow the reference beams to be "fine tuned" in order that the two images will properly align. The two rectangles which occur in every image are used to determine when the alignment is accomplished.

The lens behind the hologram serves two purposes. First, it serves to focus the collimated scene beam to a point where it can be filtered from the image. For this case, the fourier filter is in actuality a beam stop. The second and more important purpose of the lens is to transfer a real image of the holographic scene to the image plane where it can be analyzed with a traveling microscope.

A microscope assembly was constructed which provided three axis (x,y,z) coarse and fine adjustments. A LVDT transducer was attached to each axis so that electronic readout of the microscope position could be obtained. The outputs of the LVDT's were sent to three microprocessor controlled, electronic voltmeters which scaled the outputs into the true coordinates of the microscope position.

Holographic Interferometry

The arrangement of optical components for the holographic interferometer was essentially the same as the set up shown in Figure 8. However only one reference beam was used to make the interferogram. The first exposure was made with air only in the tunnel. The second exposure was made after helium had been introduced into the flow. The helium was introduced into the flow through a 1/4 inch stainless steel tube which was usually placed about 1/2 inch directly above the model nose apex. The flow of helium was regulated by installing a Lee jet orifice in the supply line from the helium bottle. The orifice size was selected to match the momentum flux of helium with that of the surrounding tunnel flow.

Two images were recorded on the same film plate with the same reference beam. The resulting interferogram, which appears when the hologram is reconstructed, exhibited a pattern of light and dark optical fringes throughout the portion of the scene containing concentrations of helium.

One important difference in the set up was the placement of a double sheet of ground glass (separated by about an inch) in the scene beam over the test section window port nearest the optics. Since each point of the ground glass plate acted like a point source, a continuum of beam direction traversed through the test scene. Upon reconstruction this meant that the scene could be examined from different points of view.

The set up without the ground glass consisted of collimated light which when viewed upon reconstruction appeared as a small bright spot twelve feet behind the model. The addition of the ground glass to the optics reduced the resolution of the reconstructed image to the point that the set up would not be useful for observing small particles. However, for interferometry the scene was much easier to view and subsequently photograph.

The reconstruction system used in the present study is shown in Figure 11. Photographs of the holographic interferogram were taken with a view camera. The camera is shown mounted on the optical rail in front of the holographic plate in Figure 11. The image was reconstructed using a HeNe laser, and the camera was focused on the virtual image behind the plate. The view camera focal length was fixed and focusing on the image was obtained by sliding the camera along the rail.

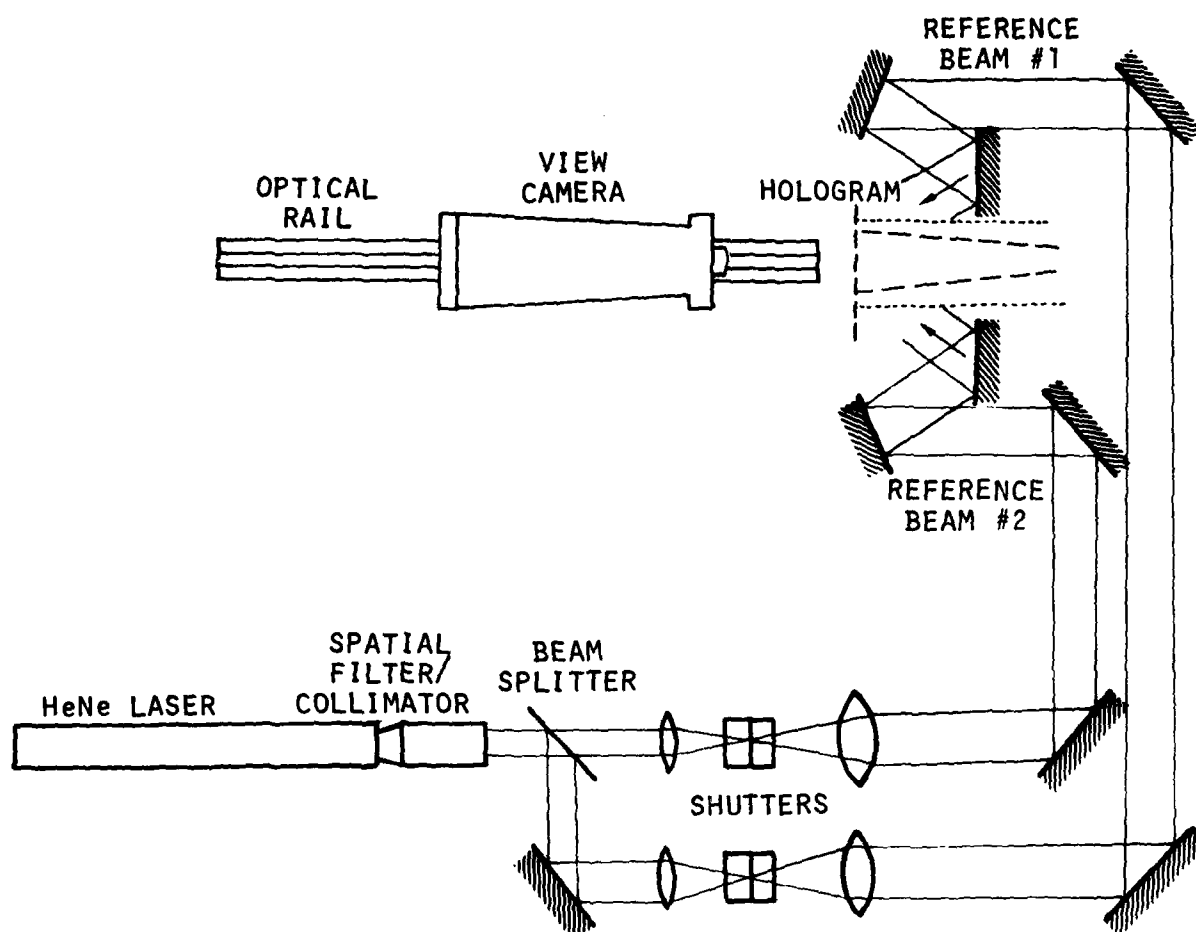


Figure 11. Camera Arrangement for Recording the Virtual Image of Reconstructed Hologram

4.0 TEST PROCEDURE

4.1 Test Conditions and Technique

The data contained in this report were obtained at free stream Mach numbers less than $M = 0.1$. The stream velocity was about 70 ft/sec and the free stream Reynolds number per foot varied from 3.7×10^5 to 4.0×10^5 .

The pressure coefficient and flow visualization data was obtained by first setting the model to the desired orientation and then adjusting the tunnel to the desired operating condition.

Holographic Interferometry

The test procedure for obtaining flow field interferograms was to fire the laser to record one image on the film plate, and then to inject helium into the flow and expose the plate a second time.

The experimental procedure involved recording the pressures either some time before or after the interferograms were made. In some cases, the pressure data was recorded directly after recording the holograms. In every case, pressures were recorded before the model was set to a new angle or roll orientation.

Rapid Double Pulse Holography

The procedure for recording the particle holograms consisted of injecting particles into stream and double pulsing the ruby laser. The first pulse followed reference beam path No. 1. The second pulse, delayed 200 microseconds from the first, followed reference beam path No. 2. The scene beam path was the same for both pulses. The particles were injected into the stream in the settling chamber just above the wind tunnel contraction section.

The particle injector consisted of a six by eight inch plexiglass box with five inlet ports arranged to create a swirling flow and exit port with an electronically controlled valve. The box was filled with hollow glass spheres which were in the range of 40 to 120 microns in size. Before each particle run, the box was pressurized with nitrogen gas. When tunnel operating conditions were reached, an electronic timer was activated which opened the valve on the particle box and then double pulsed the ruby laser

at a predetermined delay time. The delay time was calculated to allow the particles time to flow downstream to the vicinity of the model.

4.2 Data Reduction

The pressure data for all of the runs were reduced to coefficient form and integrated to give the load distribution and aerodynamic normal to side force coefficients. Photographs of the holographic interferograms were taken showing details of the vortex structure. The particle flow field was reconstructed using a HeNe laser and particles were viewed with a microscope focused on the real image. The completed test matrix is presented in Table 2.

Force and Pressure Data

The normal force, N , and pitching moment, M , on the three dimensional body of revolution were obtained by integration of the normal force per unit length dN/dX^* over the body length. Similarly the side force Y , and yawing moment, MY , were obtained by integration of the side force per unit length dY/dX^* .

The normal and side force acting on the body are

$$N = \int_0^{\ell} \frac{dN}{dX^*} dX^* \quad (15)$$

$$Y = \int_0^{\ell} \frac{dY}{dX^*} dX^* \quad (16)$$

and the pitch and yaw moments about some moment center $(X^*, Y^*, Z^*) = (\lambda d, 0, 0)$ are:

$$M_{\lambda} = \int_0^{\ell} (X^* + R^* \frac{dR^*}{dX^*}) \frac{dN}{dX^*} dX^* + d\lambda N \quad (17)$$

$$MY_{\lambda} = \int_0^{\ell} (X^* + R^* \frac{dR^*}{dX^*}) \frac{dY}{dX^*} dX^* + d\lambda Y \quad (18)$$

TABLE 2. TEST MATRIX

Model Configuration	1979 Date	Pressure		Angle of Attack, Deg.	Roll Angle, Deg.	Interferogram Plate/Point No.	Particle Plate/Point No.	Comments
		Run	Point					
N4B2	8/2	3	1-18	42.5	0-360, $\Delta\phi=22.5$			Effect of Roll Angle
	8/3	4	1		270.0			
			2		270.0			
	8/3		3		157.5			
			4		0			
	8/14				157.5			Wake Velocity Measurement: Transmission Holography
	8/18	7	1		157.5		14-3	3-D Vortex Path Measurements
			4		270.0			Set Up Holographic Interferometry
	8/18					18-8		
	8/20					18-9		
						18-10		
						18-14		
						18-16		
						20-4		
						20-7		Set Up Holographic Interferometry
N4B2 N2B1	8/20	9	1					
	8/22	13	1			20-18		3-D Vortex Path Measurements: Holographic Interferometry
	8/22	14	1			22-5		

TABLE 2. TEST MATRIX (Continued)

Model Configuration	1979 Date	Pressure		Angle of Attack, Deg.	Roll Angle, Deg.	Interferogram Plate/Point No.	Particle Plate/Point No.	Comments
		Run	Point					
N2B1	8/22	18	1	45.0	90.0	22-8 22-15	22-9 23-6 23-7 23-8 5-1 5-2 5-4	Set Up Wave Velocity Measurement: Transmission Holography
	8/22			45.0	90.0			
	8/22			45.0	90.0			
	8/23			30.0	0.0			
	8/23 9/5	19	1	30.0 20.0 20.0	0.0	6-13 6-17	6-2 6-3 6-4	Ref. Beam #2 Only
	9/5							
	9/5 9/6							
	9/6							
	9/6	20	1					
	9/6	21	1					
N2B1								

If the coordinates are non-dimensionalized by the body diameter and the forces and moments are non-dimensionalized as:

$$C_d(Z) = \frac{dN/dX^*}{1/2\rho V^2 d} \quad (19)$$

$$C_\ell(Z) = \frac{dY/dX^*}{1/2\rho V^2 d} \quad (20)$$

$$C_N = \frac{N}{1/2\rho V^2 S} \quad (21)$$

$$C_Y = \frac{Y}{1/2\rho V^2 S} \quad (22)$$

$$C_{m_0} = \frac{M}{1/2\rho V^2 S \ell} \quad (23)$$

$$C_m = C_{m_0} + \frac{\lambda}{f} C_N \quad (25)$$

$$C_{n_0} = \frac{MY}{1/2\rho V^2 S \ell} \quad (26)$$

$$C_n = C_{n_0} + \frac{\lambda}{f} C_Y \quad (27)$$

where S is the frontal area $S = \pi d^2/4$, and $R = R^*/(d/2)$ the the force and moment coefficients become,

$$C_N = \frac{4}{\pi} \int_0^f C_d dX \quad (28)$$

$$C_Y = \frac{4}{\pi} \int_0^f C_\ell \, dX \quad (29)$$

$$C_m = -\frac{4}{\pi f} \int_0^f \left(X + \frac{R}{4} \frac{dR}{dX} \right) C_d \, dX + \frac{\lambda}{f} C_N \quad (30)$$

$$C_n = -\frac{4}{\pi f} \int_0^f \left(X + \frac{R}{4} \frac{dR}{dX} \right) C_\ell \, dX + \frac{\lambda}{f} C_Y \quad (31)$$

where f is the fineness ratio, ℓ/d , and

$$C_d = \frac{1}{2} \int_0^{2\pi} C_p \cos \theta \, R \, d\theta \quad (32)$$

$$C_\ell = -\frac{1}{2} \int_0^{2\pi} C_p \sin \theta \, R \, d\theta \quad (33)$$

with the usual pressure coefficient defined as

$$C_p = \frac{p^* - p_\infty^*}{\frac{1}{2} \rho V^2} \quad (34)$$

Holographic Interferometry

Helium injection involves the use of helium to change the local index of refraction of the incompressible flow field in comparison to the reference scene of air. Double exposure holography is a technique to record the concentration of helium at some time after it has been introduced into the flow. If the helium follows flow streamlines then filament lines are recorded. A filament line is the line joining the instantaneous positions of all particles that have passed through a given point in the fluid. Smoke has been used (11,14) in the same manner where the filament lines recorded photographically.

There are at least two limitations to methods of injecting tracer fluids (or gases) to mark the filament lines that must be considered: (1) buoyancy effects, and (2) diffusion effects. Because of the low density, fluid elements of helium will tend to move towards regions of low pressure, such as vortex core.

The effect of diffusion can be estimated by approximating Fick's Law of Diffusion (15)

$$\bar{J} = D \text{ grad } \rho \quad \text{Fick's Law}$$

as

$$J \sim \frac{D\rho}{d/2}$$

where D = mass diffusivity = .11 in²/sec (He-Air)

\bar{J} = diffusive current

ρ = density

d = diameter of a streamtube

L = length of a streamtube

Now, for the effect of diffusion to be small the mass diffused through a surface during time $\Delta t = L/U$ must be less than the mass contained in the convected volume, i.e.,

$$dL \Delta t \frac{D\rho}{d/2} \ll \frac{\pi d^2}{4} L\rho$$

or

$$U_{\infty} \gg \frac{8LD}{d^2}$$

If we consider a streamtube of diameter $d = .25$ inches and length $L = 10$ inches (model length) then

$$U_{\infty} \gg 12 \text{ ft/sec}$$

for diffusion effects to be small. Since freestream velocities for the present tests were greater than about 60 ft/sec, diffusion is expected to represent a small effect.

The original objective of the experiment was to introduce helium in the core region of the body vortices so their locations could be measured in three dimensions.

To better understand the missile wake interferograms, TRW conducted a small independent interferometric investigation of the flow field behind a delta wing with a leading edge sweep angle of 76 degrees and with a root chord length of six inches. The delta wing was machined from a .25 inch aluminum plate and had sharp beveled leading edges.

Photographs of the delta wing holograms are presented in Figures 13, 14, and 15. Figure 12 shows the delta wing and missile models. The support system shown in Figure 12 was used to take the data in Figure 14. A second bent sting support system was used to take the front views in Figures 13 and 15.

Figure 15 shows the wake behind a delta wing and indicates fairly well defined cores. Other runs, Figures 13 and 14, clearly show that the concentration of helium is not confined to the core region. However, vortex structures are clearly evident. The reasons for the apparent dispersal of helium in some cases is twofold. First the helium jet has a finite thickness and therefore represents a collection of filament lines which impinge on the model surface and follow different streamlines through the fluid. The holographic interferogram is a recording of a conglomeration of filament lines. Secondly fringes are due to changes in the optical path of light traveling through the entire vortex structure. A single filament which spirals along the vortex (Ref. 14, plate 22) may appear as a diffuse vortex as in Figure 13.

Particle Tracking

The procedure for reducing the particle data from the double pulse holograms involved precisely superimposing the two images in order to obtain the velocity fields. The procedure was to first identify a particle pair, i.e., the corresponding images of the same particle from each image. This was done by "blinking" the shutter system, see Figure 10, rapidly so that the viewer saw alternating images. This approach (often used by astronomers) aids in identifying pairs. The crosshairs of the microscope are positioned over the particle image in scene #1 and the electronic readouts are zeroed. The microscope is then adjusted so that the crosshairs lie over the particle in scene #2. The electronic readouts now display the x, y and z distances traveled by the particle between the two exposures. These numbers can then be divided by the time interval between the exposures (typically

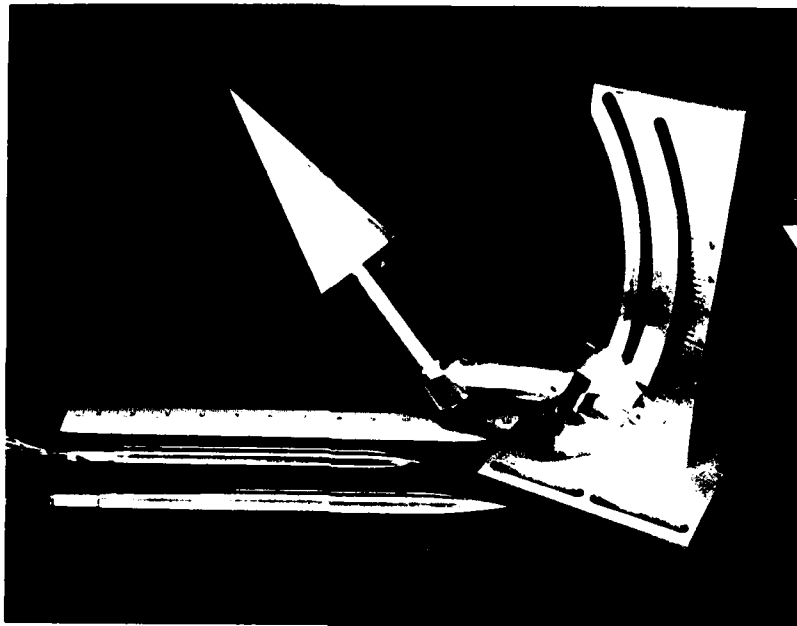


Figure 12. Wind Tunnel Models

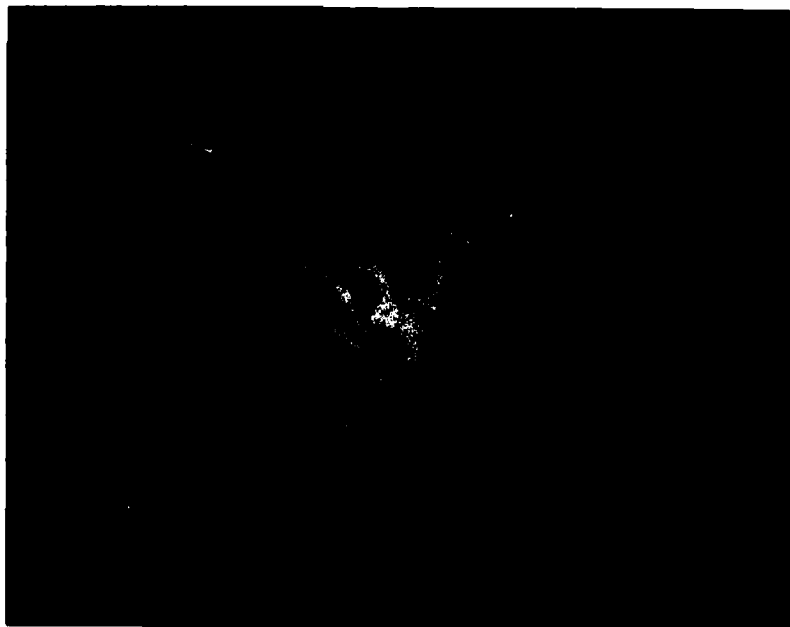


Figure 13. Delta Wing at 45 Degrees Angle of Attack,
Front View Along Body x-axis



Figure 14. Delta Wing at 45 Degrees Angle of Attack,
Side View

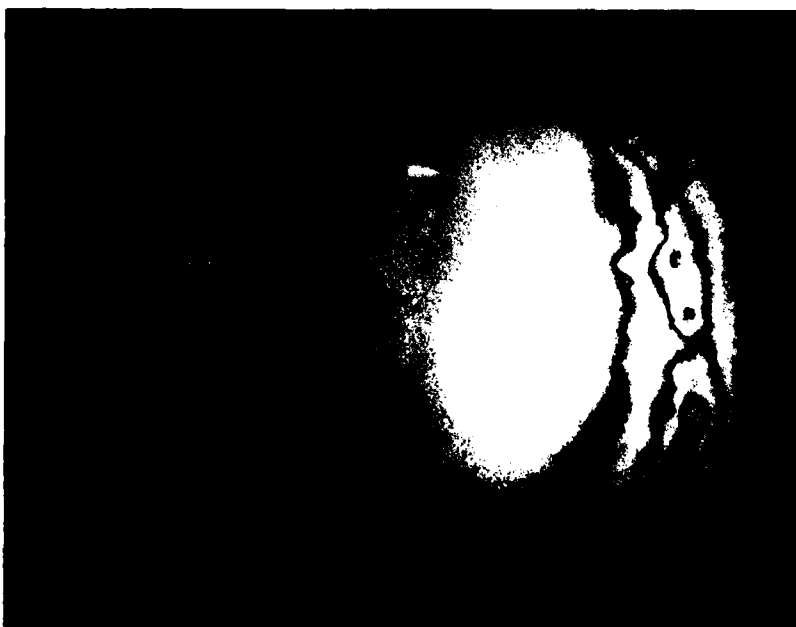


Figure 15. Delta Wing at 45 Degrees Angle of Attack,
Front View Along Free Stream Direction

200 μ sec) in order to obtain the particle velocity. This sequence is then repeated for other particles in the scene until the velocity field has been mapped.

5.0 RESULTS

Side and normal force coefficients obtained from pressure integration are presented in Figures 16 and 17 for the N4B2 body at 45 degrees angle of attack case with roll angle as a parameter. Because only three pressure stations were available the total integrated forces are only approximate. Equations (28) and (29) were numerically integrated using the trapezoidal rule over five points. At $x/d = 0$, $C_d = 0$, and $C_\ell = 0$. At $x/d = x/\ell$, C_ℓ was taken as $C_\ell = 0$, and C_d was extrapolated by choosing the value of $C_d(x/\ell) = C_d(x/\ell = \text{last station})$.

The circumferential pressure distributions are presented in Figure 18 for roll angles corresponding to maximum positive, minimum negative values of side force. The pressure distributions in Figure 18 indicate that as the roll angle varies from 45 to 270 degrees, the vortex structure assumes an almost mirror image asymmetric state. Holographic interferograms and double pulse particle holograms were taken with the roll angle fixed at $\phi = 270^\circ$ where large vortex asymmetries were apparent. The fringe patterns shown in Figure 19 were taken with the camera focused at pressure station 2 ($x/d = 4.80$). The view is looking down the missile axis from the nose. For each set of holographic interferograms taken at fixed angle of attack and roll angle, a set up hologram was made in which a pin was installed in a station 2 pressure tap. Later the set up hologram was reconstructed and the camera moved along the optical rail until the pin came into sharp focus.

The set up hologram was then replaced by the data hologram which was photographed. By sliding the camera in or out along the rail a distance corresponding to the distances between the pressure stations, fringes could also be photographed at pressure station 1 and 3. In most of the cases, the best fringes were obtained near the nose of the model where the helium was usually introduced. Fringes at station 3 were usually light because of light concentrations of helium. To facilitate comparison with the pressure distributions, the photos have been inverted so that the uniform flow is from the bottom of the picture.

The pressure distribution in Figure 20 is seen to correspond to the vortex structure as depicted in Figure 19. A strong vortex existing near

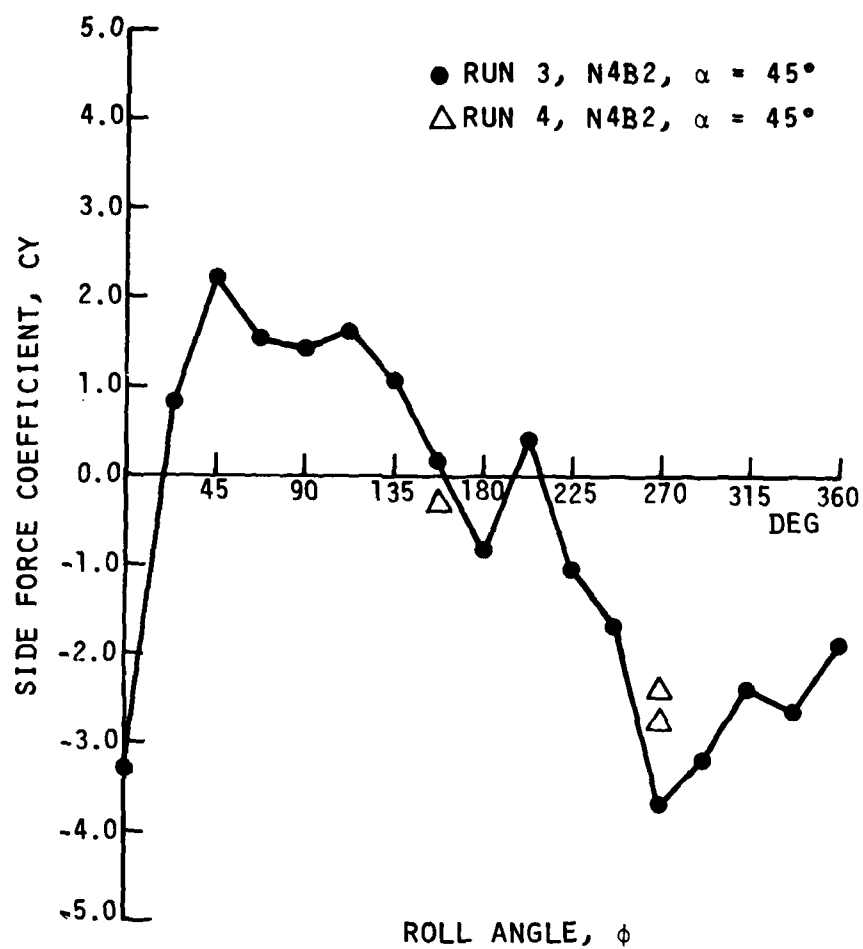


Figure 16. Effect of Roll Angle on N4B2 Side Force Coefficient.

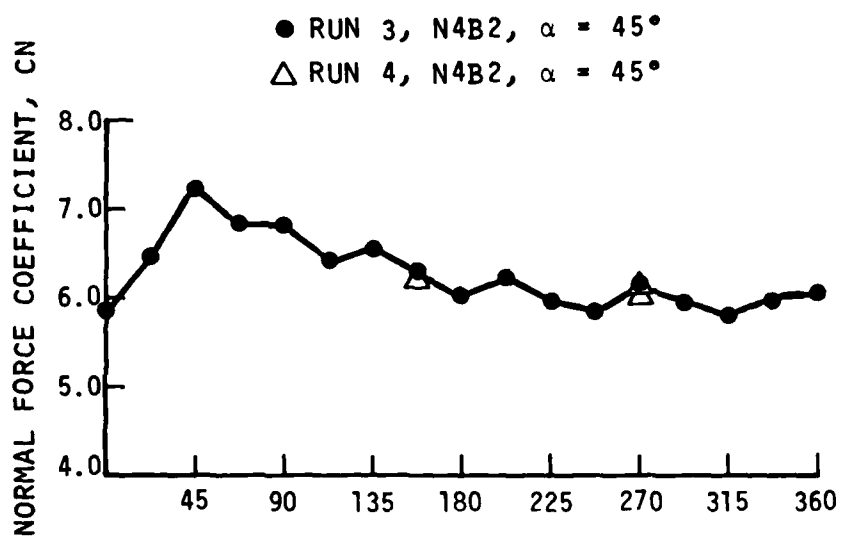


Figure 17. Effect of Roll Angle on N4B2 Normal Force Coefficient.

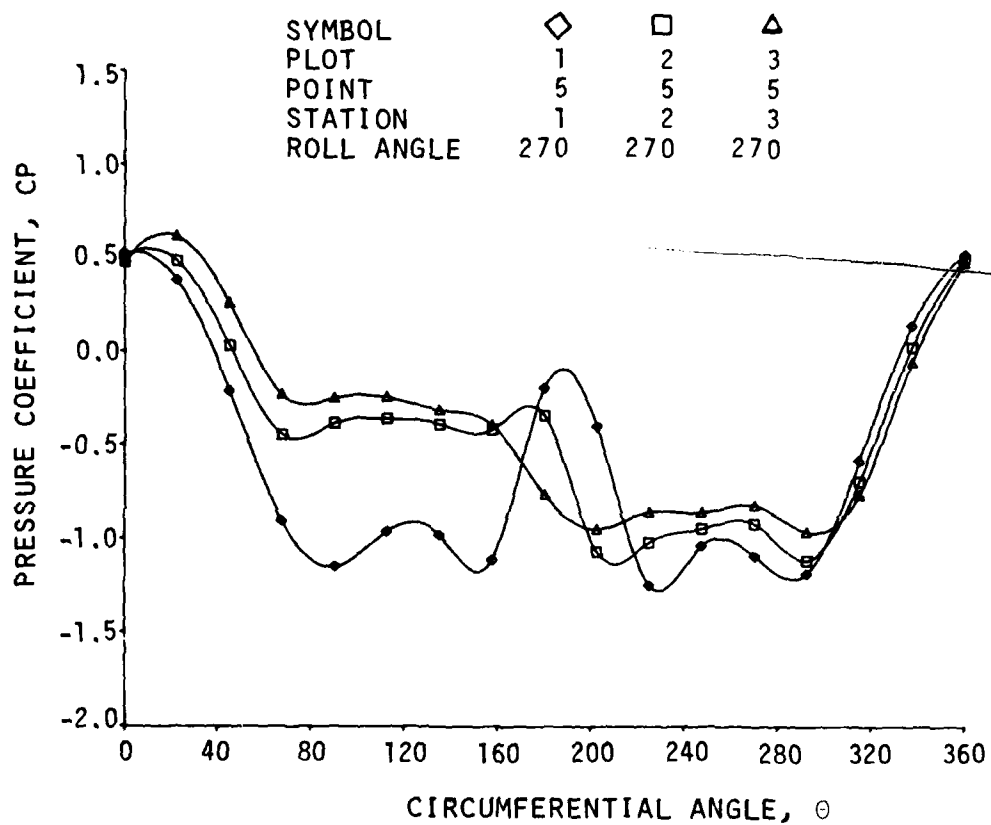


Figure 18. Pressure Distribution on N4B2.
Run 3, Angle of Attack $\alpha=45^\circ$.

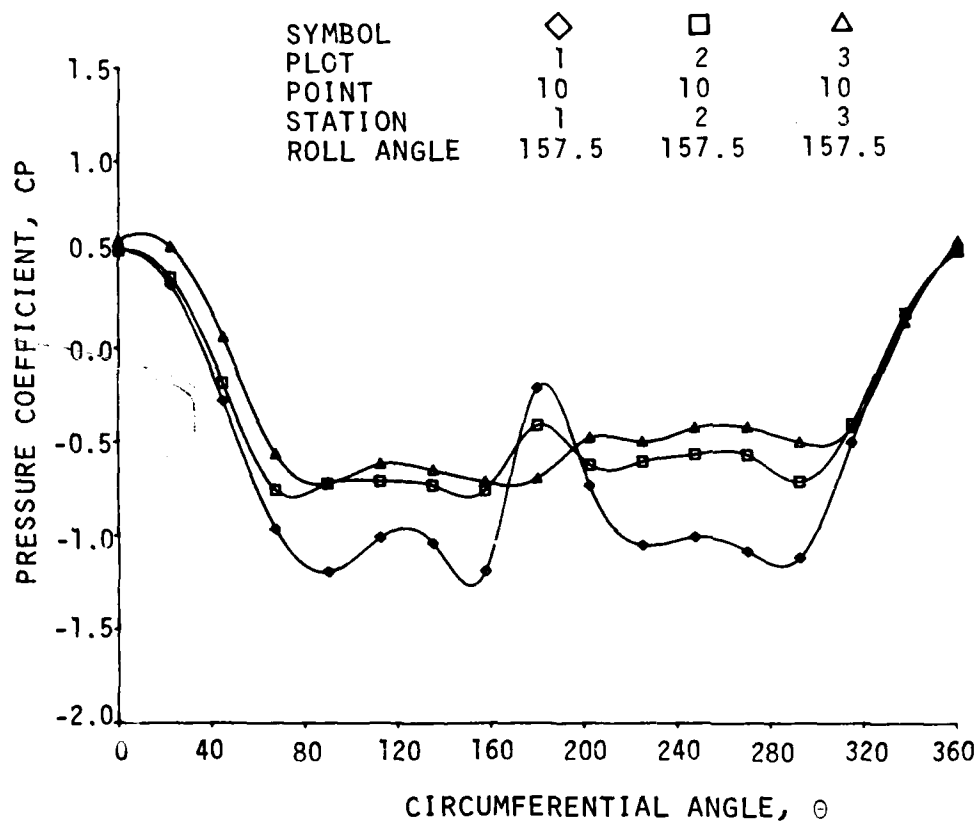


Figure 18. Pressure Distribution on N4B2,
Run 3, Angle of Attack $\alpha=45^\circ$.
(Continued)

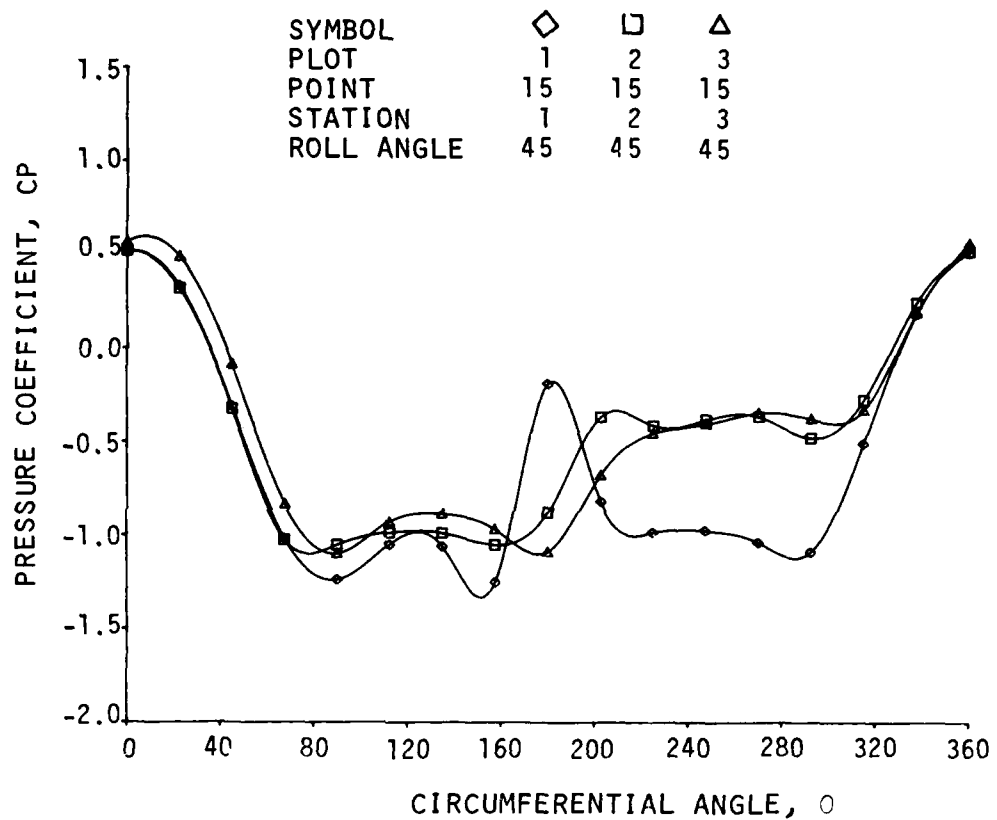


Figure 18. Pressure Distribution on N4R2,
Run 3, Angle of Attack $\alpha=45^\circ$.
(Continued)



Figure 19. N4B2 Interferogram Focused at Station 2, $x/d = 4.80$,
Angle of Attack $\alpha = 45^\circ$

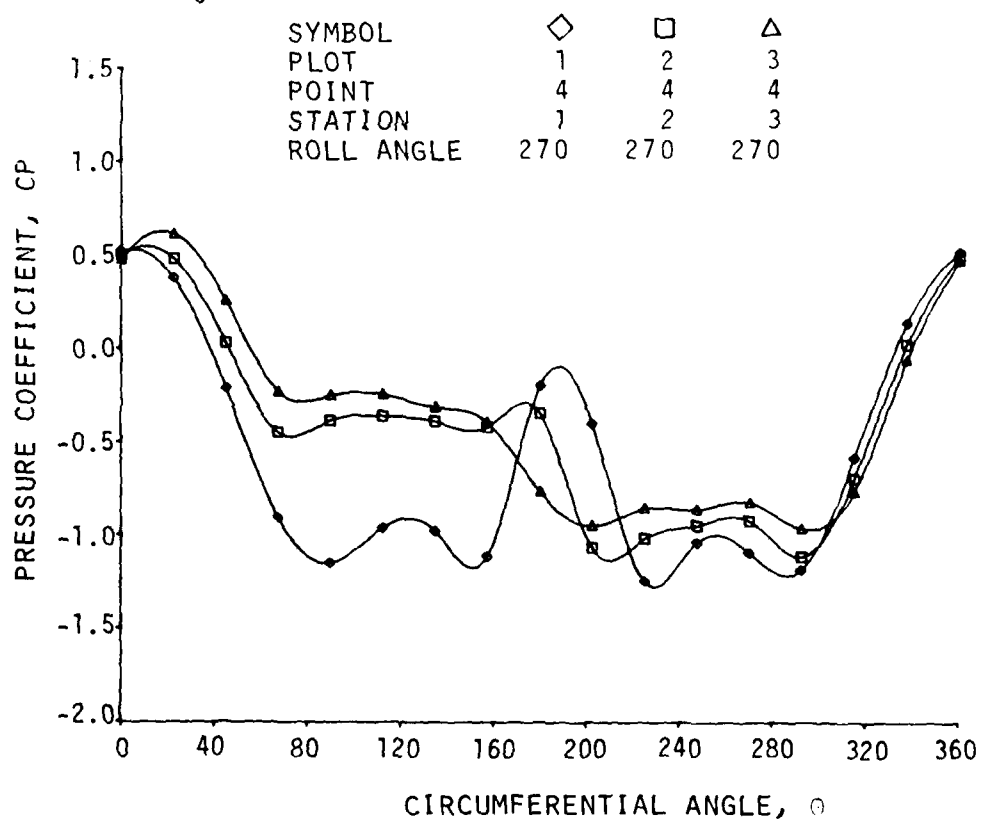


Figure 20. Pressure Distribution on N4B2,
Run 7, Angle of Attack $\alpha = 45^\circ$

the body on the right side is indicated by the fringes close to the model while on the left side the fringes indicate a more elongated weak vortex structure. The strong vortex on the right side induces high backflow velocities on the body and hence low pressures. It is worthwhile to note that Run 7 was completed several days after the initial roll survey of Run 3, and that the Run 7 pressure distribution at the 270 degrees roll position remained very nearly the same as that measured previously.

Fringe patterns for N4B2 at 50 degrees angle of attack are presented in Figure 21 for a view directly down the missile axis. The corresponding pressure distribution is presented in Figure 22. The focal plane in Figure 21a is at station 1, $x/d = 1.92$. A well formed vortex is evident near the nose on the right side. On the left side it appears that a vortex is just forming at $\theta \sim 120$ degrees. The formation of this vortex is indicated in the pressure distribution at station 1 at about $\theta = 120$ to 145 degrees. The pressures in Figure 22 indicate that the left vortex still dominates the pressure field at station 2 but is then weak or is shed and a right vortex is dominant at the last station. The fringe pattern at station 2, Figure 21b, is less defined than at station 1 probably because of a reduced concentration of helium. However the dark spot on the left side nearer the rear stagnation point indicates that a strong vortex may still exist there and account for the pressure minimum at $\theta = 90$ to 135 degrees in Figure 22 at $x/d = 4.80$.

The side force coefficient on N4B2 as a function of angle of attack is presented in Figure 23 together with values measured on the geometrically similar MX (13) model. The normal force coefficient compared with the MX data is presented in Figure 24. While the side force is of the same order of magnitude, the values of normal force computed from the measured pressure distribution are larger than were measured in the MX tests. Side force and normal force coefficient for the N2B1 body are plotted versus angle of attack in Figures 25 and 26. Again the side force coefficient falls within the range of the MX data but values of normal force coefficient appear to be high.

The local normal force coefficient distribution along N2B1 is presented in Figure 27 along with the MX data. MX pressure data, Figure 28, integrated using the data analysis routines developed for the present



Figure 21a. N4B2 Interferogram Focused at Station 1, $x/d = 1.92$,
Angle of Attack, $\alpha = 50^\circ$



Figure 21b. N4B2 Interferogram Focused at Station 2, $x/d = 4.80$,
Angle of Attack, $\alpha = 50^\circ$

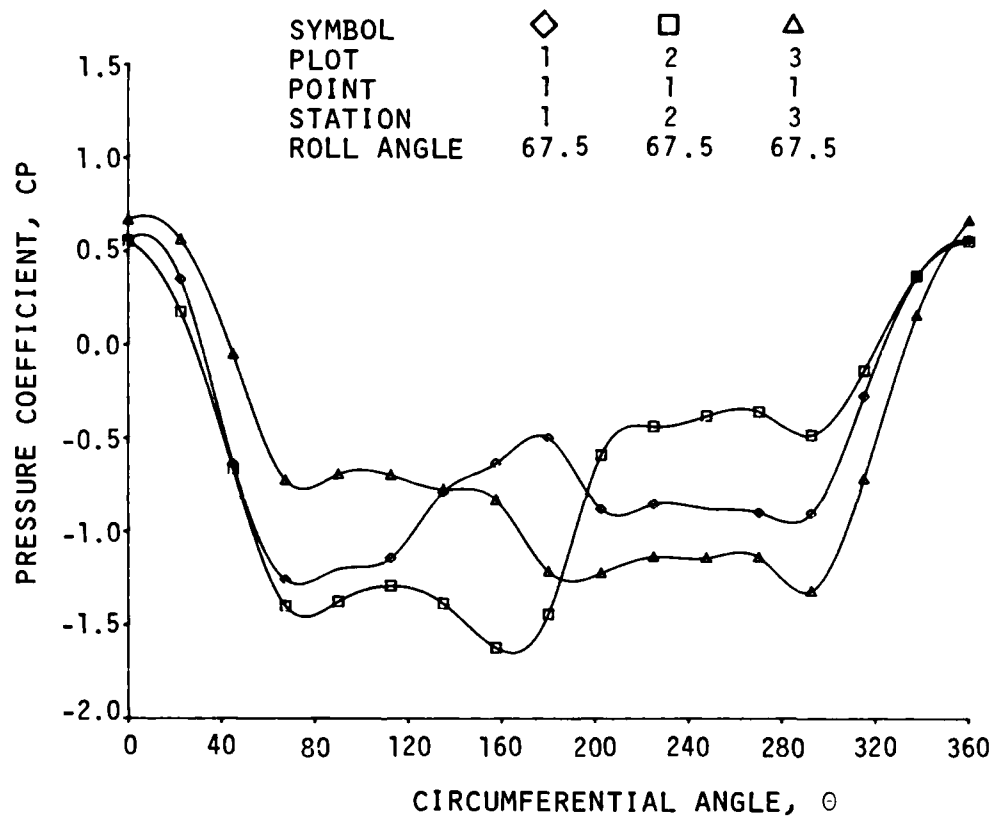


Figure 22. Pressure Distribution on N4B2,
Run 9, Angle of Attack $\alpha=50^\circ$.

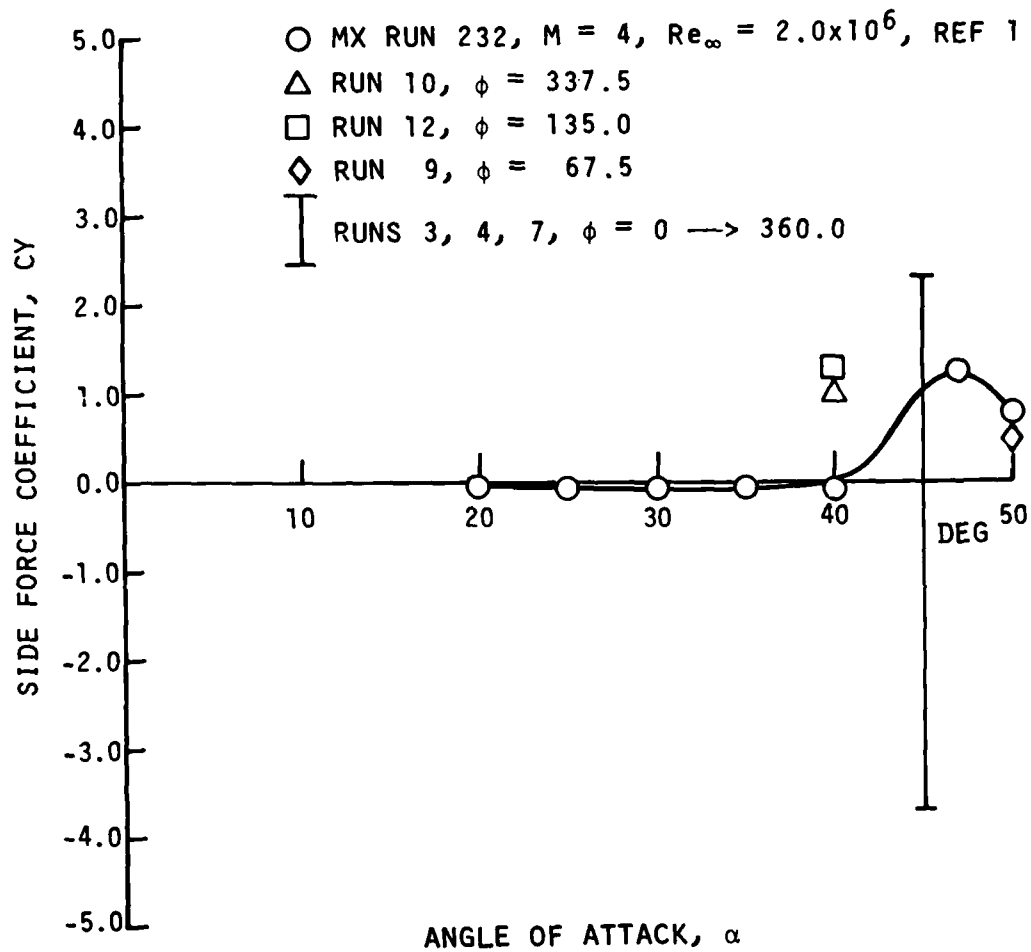


Figure 23. N4B2 Side Force Coefficient Variation With Angle of Attack.

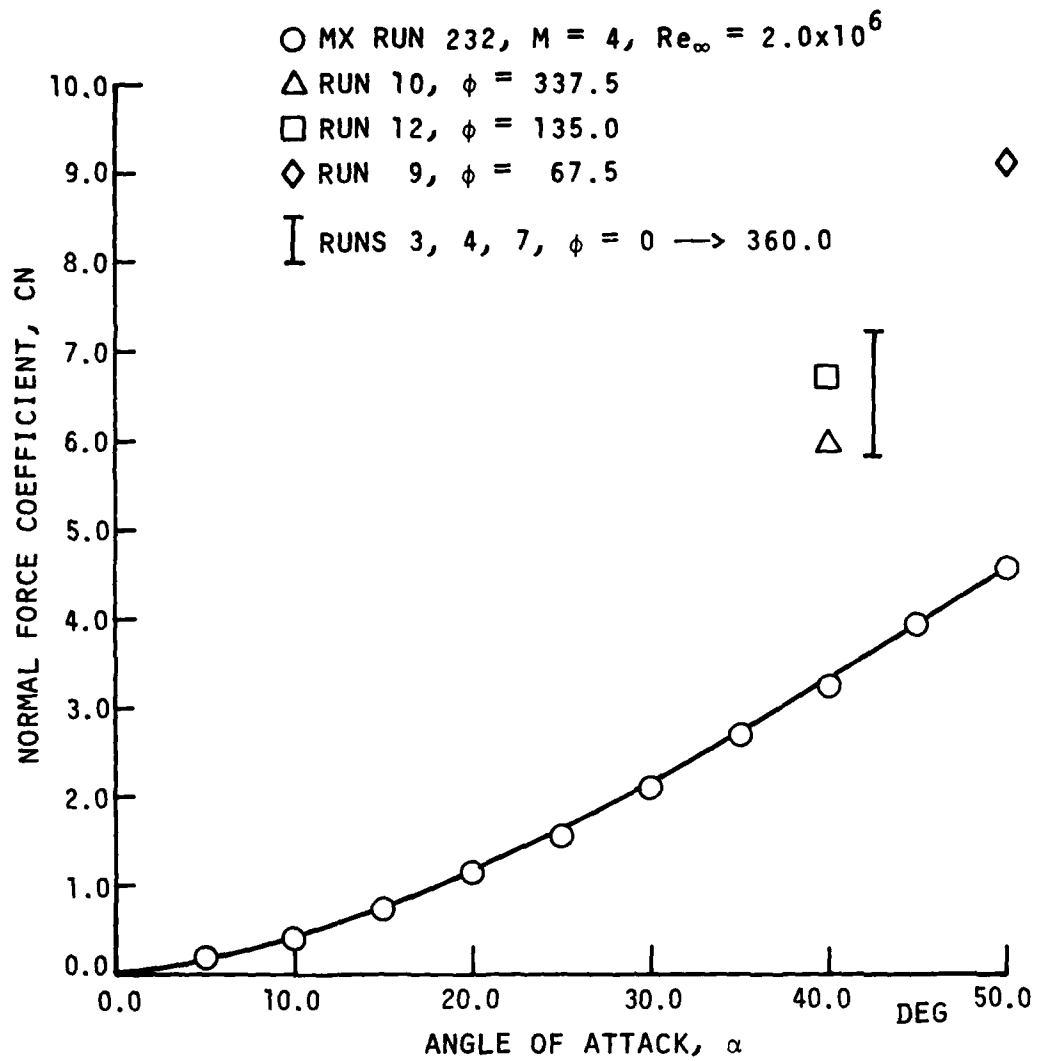


Figure 24. N4B2 Normal Force Coefficient Variation With Angle of Attack.

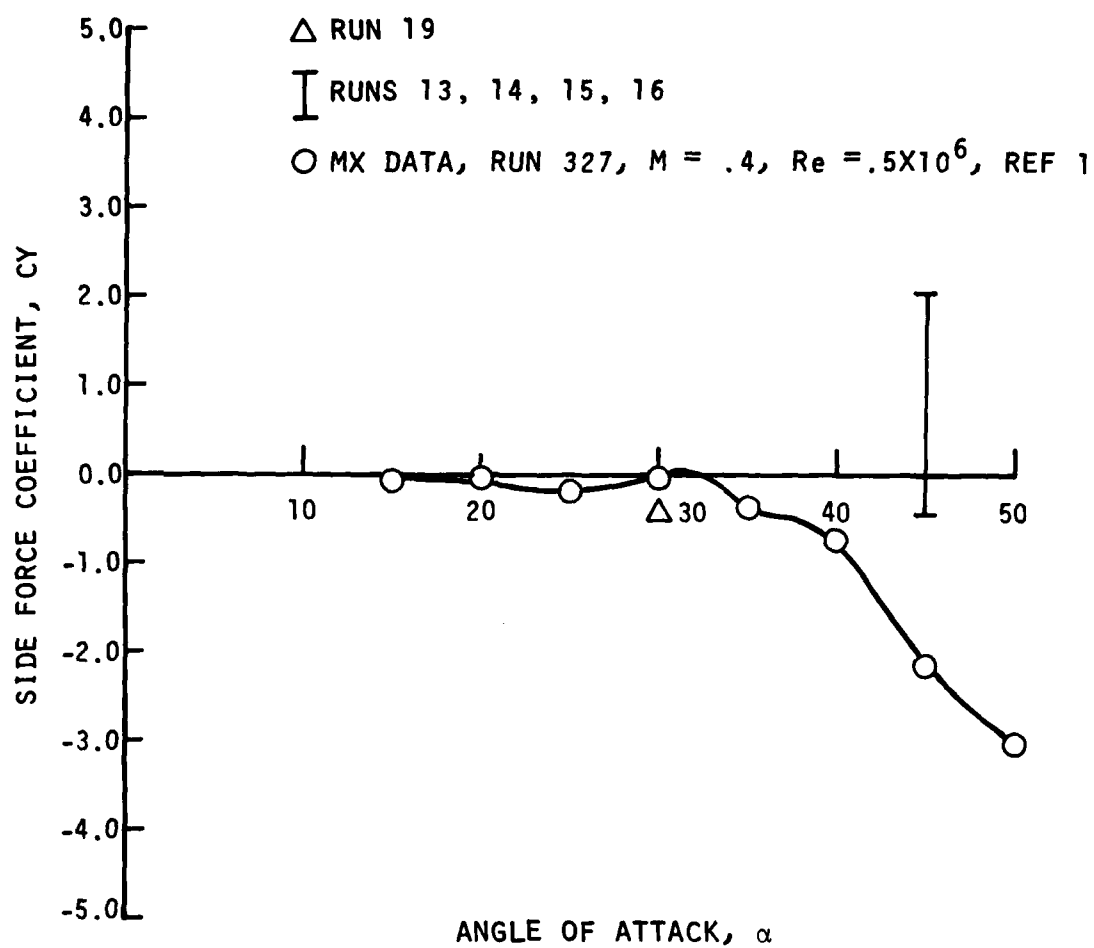


Figure 25. N2B1 Side Force Coefficient Variation With Angle of Attack.

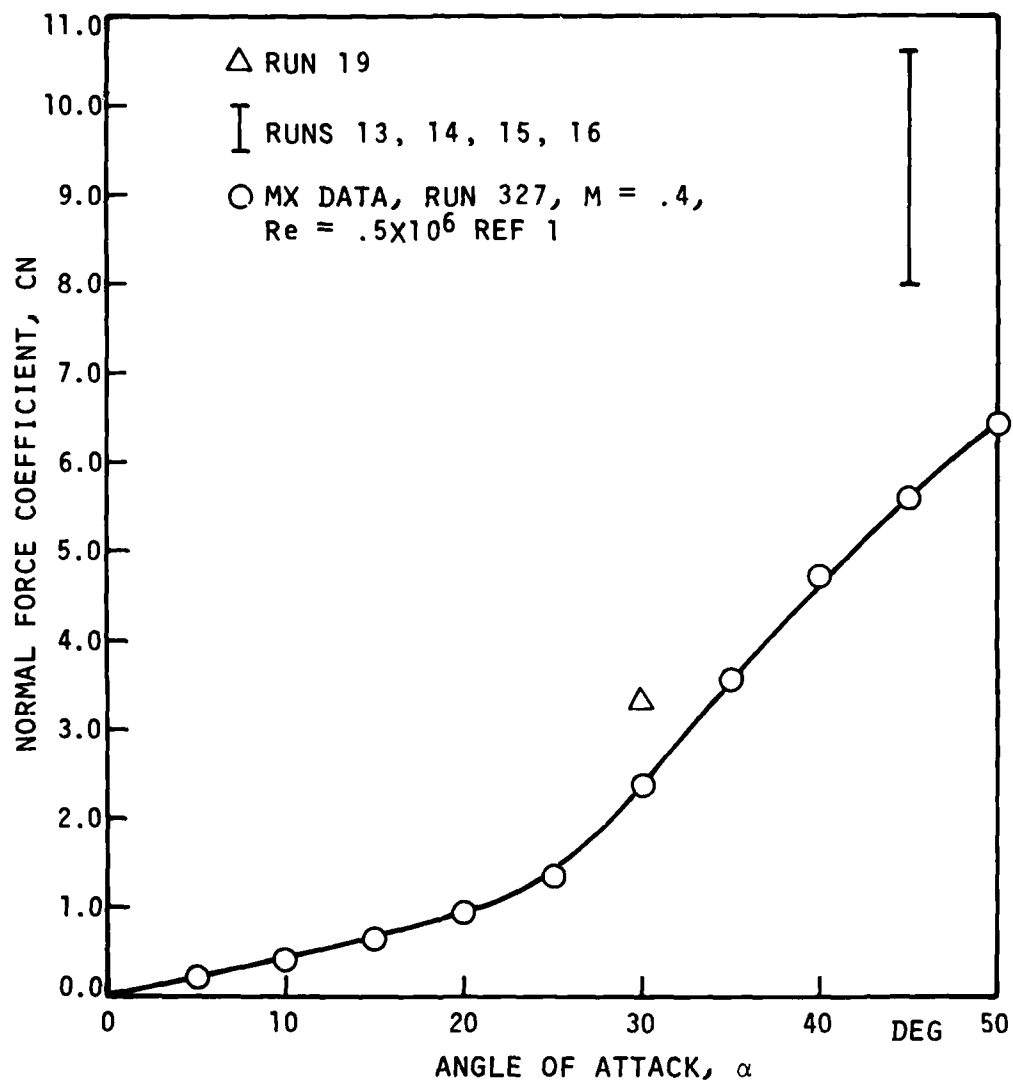


Figure 26. N2B1 Normal Force Coefficient Variation With Angle of Attack.

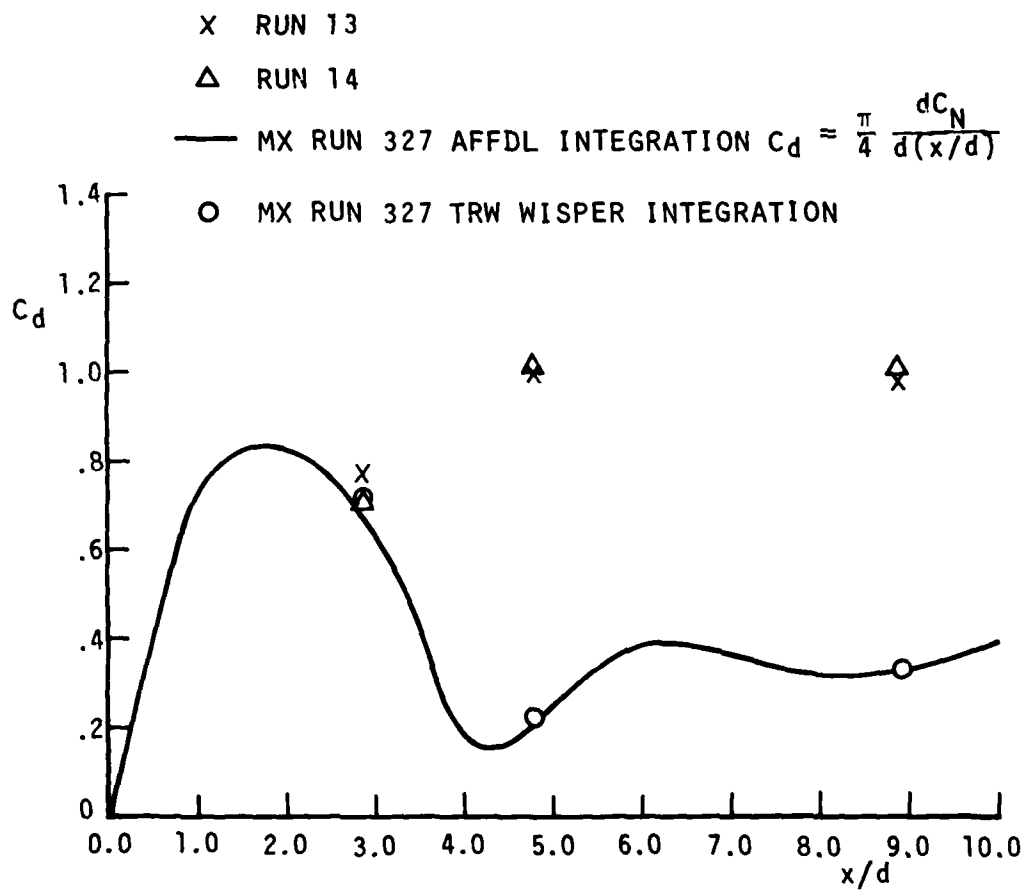


Figure 27. Normal Force Distribution on N2B1 at 45 Degrees Angle of Attack.

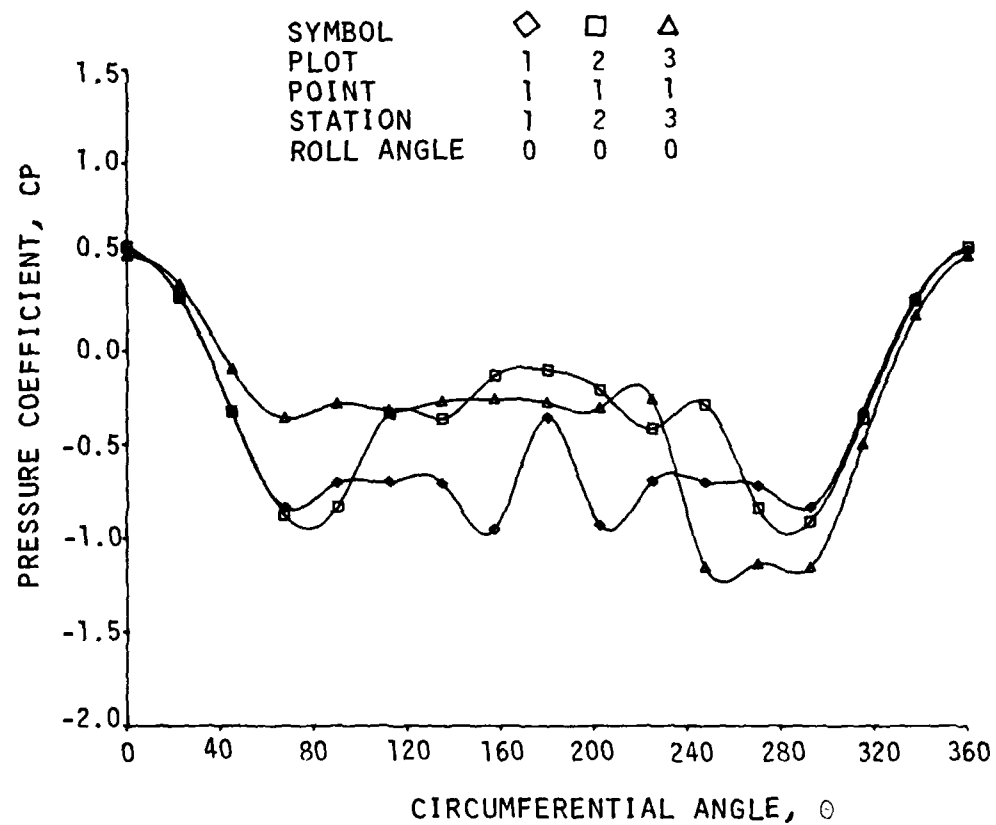


Figure 28. Pressure Distribution on N2B1, MX
Run 327, Angle of Attack $\alpha = 45^\circ$.

program yielded results almost identical to the values of local normal force obtained by AFFDL. At the first pressure station the value of local normal force in the present work agrees closely with the AFFDL MX value. However, the calculated values of local normal force at station 2 and 3 for the present experiment is much higher than the values obtained in the MX work. As seen in the pressure distribution plots for the 45 degree angle of attack case, Figure 29, the present values are much lower over the lee side of the missile.

A photograph of the fringe pattern looking down the x-axis of N2B1 at 45 degrees angle of attack is presented in Figure 30. The fringes for this case were very light and difficult to photograph. However, upon close inspection, two vortex cores can be seen very close to the body surface.

N2B1 pressure distributions at 30 and 20 degrees angle of attack are presented in Figures 31 and 32. An interferogram of the N2B1 model at 30 degrees angle of attack is presented in Figure 33. The body is difficult to distinguish in the photograph because the model blocks the laser light. However, the model is yawed toward the top window as it appears in the installation photograph, Figure 2.

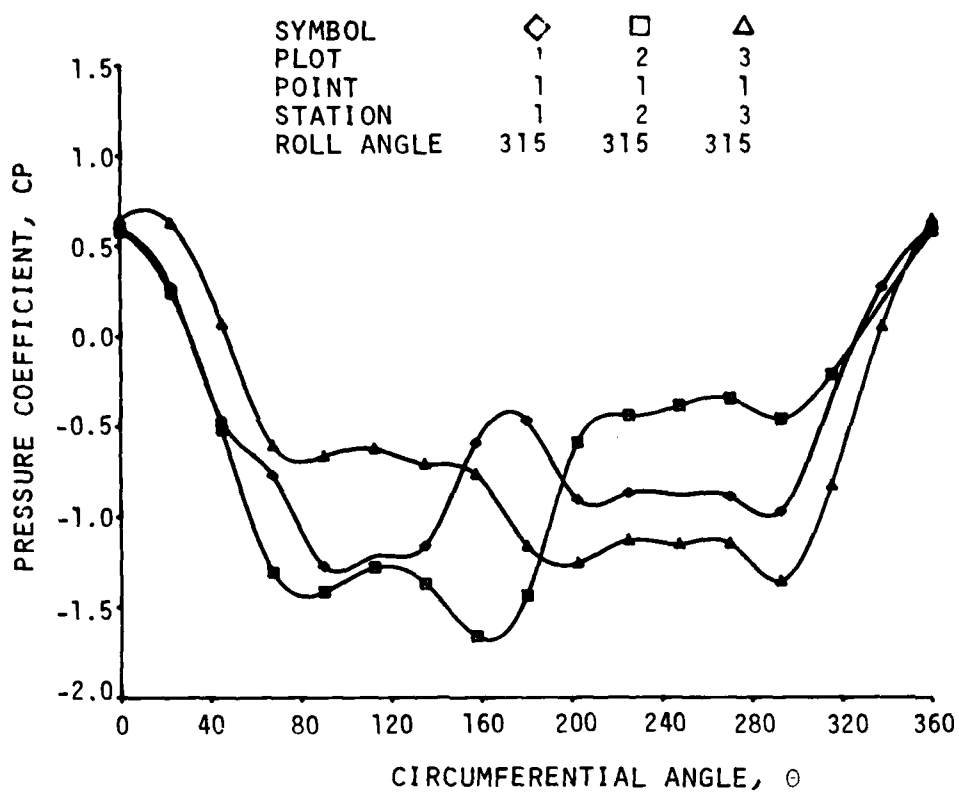


Figure 29. Pressure Distribution on N2B1, Run 13, Angle of Attack $\alpha = 45^\circ$



Figure 30. N2B1 Interferogram Focused at Station 1, $x/d = 2.83$, Angle of Attack, $\alpha = 45^\circ$

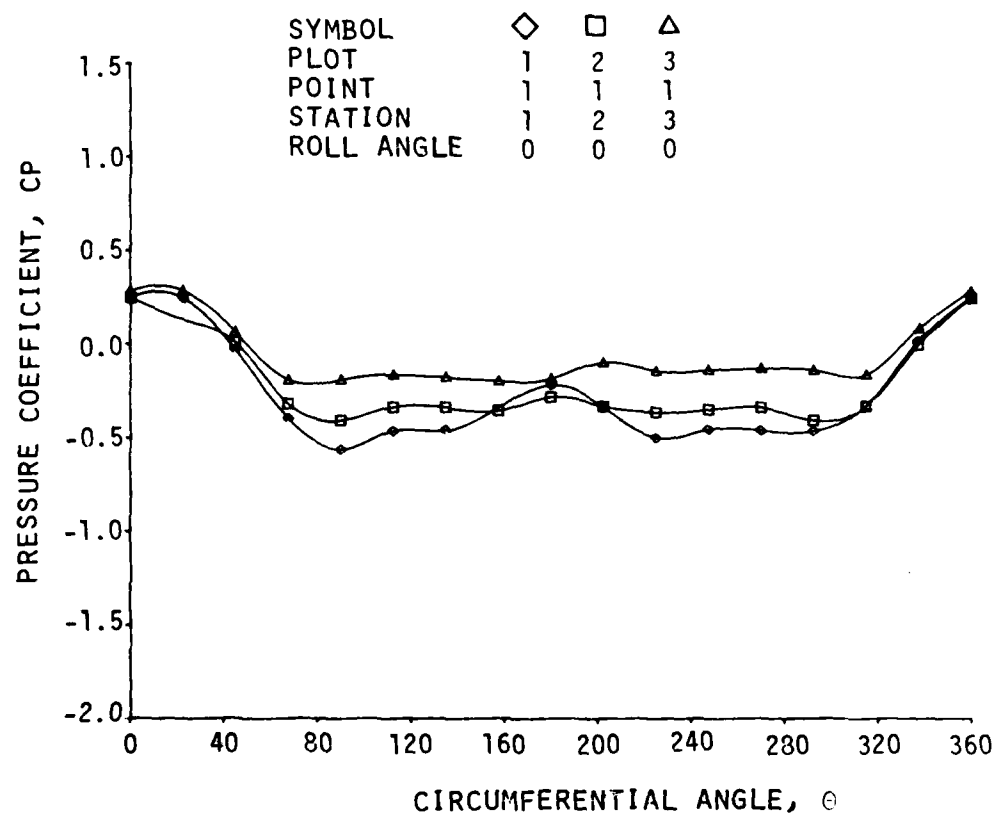


Figure 31. Pressure Distribution on N2B1,
Run 18, Angle of Attack $\alpha=30^\circ$.

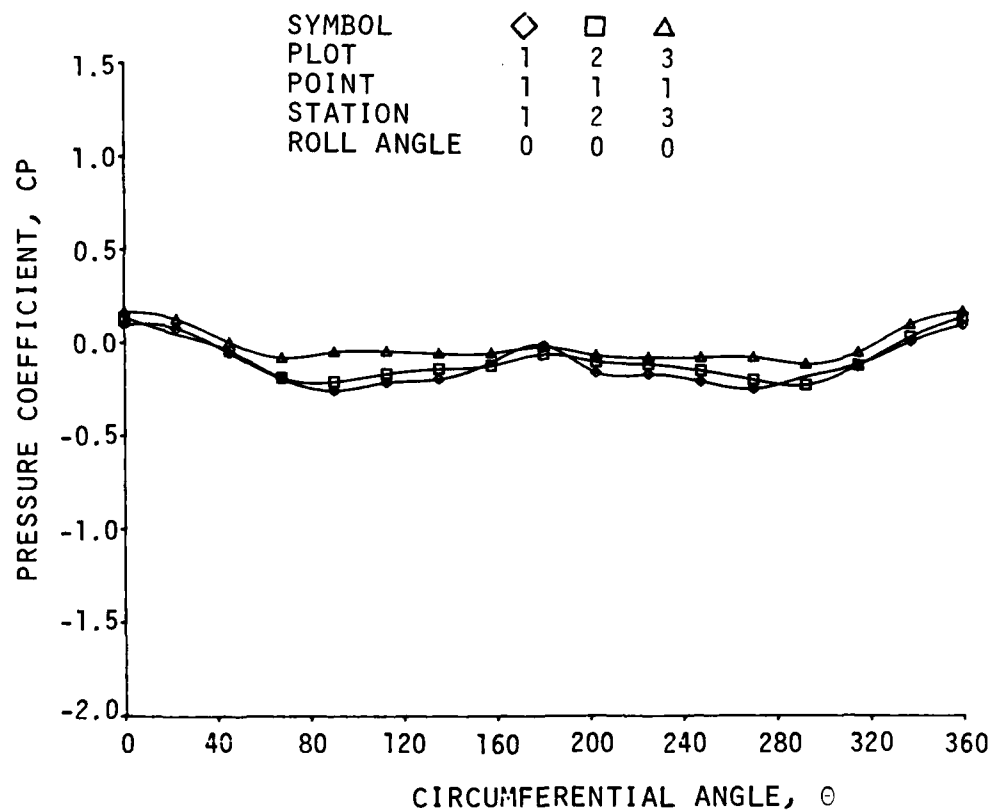


Figure 32. Pressure Distribution on N2B1,
Run 21, Angle of Attack $\alpha=20^\circ$.



Figure 33. N2B1 Interferogram Taken From the Side,
Angle of Attack, $\alpha = 30^\circ$

6.0 DISCUSSION

Two holographic flow visualization techniques were used to examine the high angle of attack flow field. Holographic interferometry was used to visualize the vortex structure. Rapid double pulse holography of a flow seeded with small particles was used to record the spatial distribution of the particles at two instants in time so that the three dimensional velocity field could be later mapped.

Objectives of the present effort were:

1. To measure the u , v , w components in the vortex wake
2. To determine the unsteady nature of the vortex flows
3. To measure the x , y , z locations of the vortex cores
4. To determine the structure of the wake as affected by the roll angle and nose geometry
5. To measure surface pressures.

Objective 5 was successful and objectives 3 and 4 were partially successful in a qualitative sense. Objectives 1 and 2 were not met.

The initial purpose of using holographic interferometry was to develop a method which could be used to locate the position of the vortex core in three dimensional space. The idea was that helium would be entrained into the vortex core and appear as a tight band of fringes which could be observed. In practice, helium was entrained not only into the core region of the vortex, but into the entire vortex structure. Missile flow field fringe patterns were obtained which were difficult to interpret.

To gain a better understanding of the phenomena the interferometric technique was used to visualize the flow over a delta wing at angle of attack. Because the delta wing vortex structure is better defined experimentally and more easily modeled mathematically, the observed fringe pattern was easier to interpret.

Interferograms of the delta wing flow were obtained which clearly visualized the entire vortex structure. In chordwise views core locations were apparent. However, because fringes are due to changes in the optical path of the light traveling through the entire structure, the spanwise location of the cores was not obvious. Views looking from the side appeared much as the side views of the missile flow. Again because helium was

entrained into the entire structure and not just the core, and because the fringes represent the integral over the physical path length of all the changes in index of refraction, core locations could not be obtained directly from the photographs. It is important to note that the three dimensional information is contained in the holograms. However, the analysis required to extract that information is formidable. In fact, for complicated three dimensional flows of this type, no general method has, to our knowledge so far been developed.

A dual reference beam transmission holocamera was set up to record the flow seeded with small particles.

A "quick look" reconstruction system was set to permit either view to be studied, but it was not possible to superimpose both holograms and view the composite image. Without this capability, positive identification of particles could not be made. Therefore, the quality of the data was not known precisely until after the test series was completed. Thus, it was not possible to close the loop and make the changes in the test procedure which were indicated by the data obtained.

During the data reduction phase of the program, a number of problems with the data format became apparent. Several changes in the test techniques (for the most part minor) were indicated. A discussion of the logic behind these test techniques and the desirable changes is presented below. It is hoped that this will serve as a useful guide for future experiments in this area.

A light field transmission holographic technique was chosen because of the flexibility it allows during the data reduction phase. A collimated scene beam was used to illuminate the test volume. A number of options are then available for the selection of viewing optics. The choice is governed mainly by the desired method for reducing the data. For example, magnification lenses may be used to improve the resolution, transfer lenses to produce a real image or a field stop to filter out the background illumination.

In practice, the hologram can be placed at any point in the optical path (after the test volume). When optics are positioned between the test

volume and the hologram, the data reduction technique is locked in. By positioning the hologram directly in the collimated scene beam with no optics between it and the scene, total flexibility in choosing the reconstruction technique is retained. It was felt that this flexibility was essential due to the uncertainties in the quality of the data which would later be obtained.

The flexibility, however, is not without a cost. The bright field hologram has a very poor signal-to-noise ratio. While fourier filtering can be (and was) used to filter out the background noise, the efficiency of this process is higher if performed before the hologram. Furthermore, the efficiency of the holographic recording is enhanced and its noise reduced if a lower intensity scene beam is used. Another related problem arises from the fact that shadow regions exist about the model which are equivalent to dark field holograms. This results in some confusion in the data interpretation. As it turned out, the particle data could only be read against a dark field. Therefore, it would have been better had the filtering process occurred ahead of the hologram. This could have been accomplished by focusing the scene beam onto a field stop located immediately in front of the hologram.

A second problem area relates back to the symmetry of the experimental set up. The efficiency and signal-to-noise ratio of the holographic recording is a function of the angles between the scene and reference beams and between these beams and the hologram itself. In order to meet the requirements that the two holographic images superimpose precisely and have similar intensities, a symmetrical optical arrangement was chosen. Each reference beam impinged on the hologram at precisely the same angle, but from opposite sides. It was found that many of the holograms contained "ghost" images of a bright point at infinity which could not be focused. These "ghost" images tended to lie over the true scene image and tended to confuse the reconstruction process. It was determined that these "ghosts" were due to second order diffraction effects from the other reference beam. The symmetry caused this diffracted "ghost" to lie over the true scene. This problem would be minimized by utilizing a non-symmetrical optical arrangement, i.e., having the two reference beams impinge at different angles. This approach

would require additional care that the two images were sufficiently similar to allow their proper superposition.

The precise superpositioning of the two holographic images which are required to reduce the particle data is another area where improvement can be made. The method chosen employed the use of two recticles. One was mounted on the outer side of each of the wind tunnel windows (actually about 1/2 inch from the window and tilted to be perpendicular to the scene beam). These were positioned to be near the edge of the scene so that they could be seen when viewing the holograms but not interfere with the data reduction. In practice, it was difficult to set the reconstruction optics to have the required resolution and clarity over so large a scene volume. A better approach would have been to make alignment holograms wherein the recticles were positioned in the volume which the particles would occupy. The reconstruction optics could then be aligned using this hologram (a new one would be required with each change in model position or optics adjustment). The data hologram could then be substituted into the reconstruction set up. A similar approach was used in the interferometric tests where a pin was inserted into a pressure tap on the model for a set up hologram in order to later focus the camera into the plane of the pressure taps.

Although the velocity field was not mapped in this study with the recommended changes the technique could be used to determine the three-dimensional velocity field for aerodynamic flow of this type. However, at the present state-of-the-art, the usefulness of such a method is limited by restrictions on particle size and data reduction techniques.

For particles to follow streamlines in a vortex flow, small particle sizes $\phi \lesssim 5$ microns are required. However particles that are too small scatter less light and are difficult to record. The resolution after reconstruction depends upon the resolution by the photographic emulsion and importantly on the distance between the particle and recording plane. At present, particle sizes of about 100 microns seem to be an optimum. Particles this large will probably not track streamlines accurately. Also, as demonstrated in the present study, even 100 micron particles may not be that easy to record for a practical wind tunnel study where dimensions of the optical arrangement are constrained.

For practical aerodynamic wind tunnel studies very large amounts of information can be recorded in a very short period of time using pulsed laser holography. Because the procedure for extracting the data is visual, i.e., each particle must be resolved optically and its position recorded, data reduction is a problem. The importance of this aspect of the work should not be underestimated by anyone contemplating using these techniques. Attempting to reduce data manually using a microscope (or telescope) to locate individual particles is tedious, expensive, and nearly impossible for large amounts of data. An automated system for identifying particles and recording their location will be required for practical application of the method.

7.0 CONCLUSIONS AND RECOMMENDATIONS

Two ogive cylinder wind tunnel pressure models were tested in TRW's low speed wind tunnel. Measured pressure distributions and vortex asymmetries were sensitive to model roll orientation for constant tunnel conditions and model attitude. Values of side force coefficient obtained by integrating the surface pressure distribution agreed well with previous experimental results. Values of normal force coefficient were higher than that obtained by other investigators.

Holographic interferometry was used to visualize the three dimensional structure of the vortex flow field. Fringe patterns viewed from the side (out of the angle of attack plane) were difficult to interpret in terms of vortex core locations. Helium was entrained into the entire vortex structure and not restricted to the area of the core. Vortex cores could be seen in views taken in the angle of attack plane looking directly down the missile axis. Qualitative agreement was obtained between core location and the measured pressure distributions. Further analysis of the data is required to obtain the three dimensional position of the cores.

Dual exposure holograms of the particle seeded flow field were taken by rapidly double pulsing a ruby laser. The technique used two separate reference beams, one for each exposure. Reconstruction of the scene with one reference beam revealed particles with a resolution of about 50 microns. Problems encountered in reconstructing with the second reference beam prevented reducing the spatial information to three-dimensional velocity measurements with the present optical apparatus. Particle identification was difficult due to extraneous noise in the hologram, and due to shadows created by the model.

Practical applications of the holographic methods for general aerodynamic flows such as the high angle of attack vortex wake flow involves a number of difficulties which may be overcome but with considerable effort. A basic concern with tracking particles using holography or any other seeded flow technique is that the particles follow the flow. Small particles will follow the flow but are difficult to resolve in the reconstructed scene. Reducing the information recorded in three-dimensional space to flow field velocities while trivial theoretically presents a problem

for large amounts of data. An automated particle identification and recording technique is required to make holographic velocimetry practical for measuring general aerodynamic flow fields.

REFERENCES

1. Lamont, P. J. and Hunt, B. L., "Pressure and Force Distribution on a Sharp-Nosed Circular Cylinder at Large Angles of Inclination in a Uniform Subsonic Stream," Journal of Fluid Mechanics, Vol. 76, 1976, pp. 519-559.
2. Hunt, B. L. and Dexter, P. C., "Pressures on a Slender Body at High Angle of Attack in a Very Low Turbulence Level Air Stream," AGARD Conference Proceedings No. 247, Fluid Dynamics Panel Symposium, October 1978.
3. Oberkampf, W. L., Owen, F. K. and Shivananda, T. P., "Experimental Investigation of the Asymmetric Body Vortex Wake," AIAA Paper No. 80-0174, 18th Aerospace Sciences Meeting, Pasadena, CA, January 1980.
4. Deffenbaugh, F. D. and Koerner, W. G., "Asymmetric Vortex Wake Development on Missiles at High Angles of Attack," AIAA J. Spacecraft and Rockets, Vol. 14, No. 3, March 1977, pp. 155-162.
5. Clark, W. H. and Nelson, R. C., "Body Vortex Formation on Missiles at High Angles of Attack," AIAA Paper No. 76-65, AIAA 14th Aerospace Sciences Meeting, Washington, D.C., January 1976.
6. Fidler, J. E., Nielsen, J. N. and Schwind, R. G., "An Investigation of Slender-Body Wake Vortices," AIAA Paper No. 77-7, AIAA 15th Aerospace Sciences Meeting, Los Angeles, CA, January 1977.
7. Owen, F. K., "Wake Vortex Measurements of Bodies at High Angles of Attack," AIAA Paper No. 78-23, AIAA 16th Aerospace Sciences Meeting, Huntsville, Alabama, January 1978.
8. Wardlaw, A. B. and Yanta, W. J., "The Flow Field About, and Forces on Slender Bodies at High Angles of Attack," AIAA Paper No. 80-0184, AIAA 18th Aerospace Sciences Meeting, Pasadena, CA, 1980.
9. George, D., Briones, R. A. and Wuerker, R. F., "Holography of Solid Propellant Combustion," AIAA/SAE 13th Joint Propulsion Meeting, July 1977, Orlando, FL.
10. Smith, H. M., Principles of Holography, Second Edition John Wiley & Sons, New York, 1975.
11. Merzkirch, W., Flow Visualization, Academic Press, New York and London, 1974.
12. Wuerker, R. F., "Holographic Interferometry," Proc. ICO Conference on Optical Methods in Scientific and Industrial Measurements, Tokyo, August 1974.

REFERENCES (Continued)

13. Baker, D. C. and Reichenau, D. E. A., "Aerodynamic Characteristics of an MX Missile at Free-Stream Mach Numbers from .3 to 1.3 and Angles of Attack up to 180 Degrees," Arnold Engineering Development Center, Arnold AFB, Tenn., AEDC-TR-75-34, April 1975.
14. Batchelor, G. K., An Introduction to Fluid Dynamics, Cambridge University Press, 1967, Plate 22.
15. Bird, B. R., Stewart, W. E. and Lightfoot, E. N., Transport Phenomena, John Wiley and Sons, New York, 1960, p. 502.